Water Resources Research

RESEARCH ARTICLE
10.1029/2020WR028515

# Coupled Morphodynamics of River Bifurcations and Confluences

**Niccolò Ragno**[1,2], **Marco Redolfi**[2], **and Marco Tubino**[2]

[1]Department of Civil, Chemical and Environmental Engineering, University of Genoa, Genova, Italy, [2]Department of Civil, Environmental and Mechanical Engineering, University of Trento, Trento, Italy

**Key Points:**

- The dominating branch of a channel confluence shows a higher water level, depending on the square of the Froude number
- The confluence exerts a negative feedback on the upstream bifurcation, which promotes the stability of the system
- The bifurcation-confluence system can be stable even when the bedload steering at the bifurcation is very weak

**Supporting Information:**

- Supporting Information S1

**Correspondence to:**
N. Ragno,
niccolo.ragno@edu.unige.it

**Citation:**
Ragno, N., Redolfi, M., & Tubino, M. (2021). Coupled morphodynamics of river bifurcations and confluences. *Water Resources Research*, *57*, e2020WR028515. https://doi.org/10.1029/2020WR028515

Received 30 JUL 2020
Accepted 18 NOV 2020



**Abstract** Multithread fluvial environments like anastomosing and braided rivers are fundamentally directed by the continuous concatenation of channel bifurcations and confluences, which distribute flow and sediment among different branches that are reconnecting further downstream. A large number of theoretical, experimental, and numerical studies conducted in the last two decades have provided a clear picture of stability conditions for river bifurcations. However, most analyses are focused on the dynamics of bifurcations alone, ignoring the possible mutual interaction with downstream confluences. In this work, we study the morphodynamic equilibrium and stability conditions of a bifurcation-confluence loop, where flow splits in two secondary anabranches that rejoin after a prescribed distance. Through the formulation of a novel theoretical model for mobile bed confluences, we show that the dominating anabranch (i.e., that carrying most discharge) is subject to an increase of the water surface elevation that is proportional to the square of the Froude number. This effect causes a decrease of the slope of the dominating anabranch, which acts as a negative feedback that increases the stability of the bifurcation-confluence system. A linear analysis of the coupled model reveals that the stabilizing effect exerted by the confluence depends on the ratio between the length of the anabranches and the average water depth, independently of channel slope and Froude number. Ultimately, this effect is potentially able to stabilize the loop even when the sediment is mainly transported in suspension, a condition which makes the classic stabilizing mechanism (i.e., the topographic effect at the bifurcation node) practically ineffective.

## 1. Introduction

The study of multithread systems like braided and anastomosing rivers, deltas, alluvial fans, represents a fascinating topic in the vast world of river patterns. The flow splits around exposed bars, islands, ridges, and often reconnects a little further downstream. Water and sediment partition in the bifurcates has a fundamental control of the river morphological evolution and ecological functionality (Ashmore, 2013; Nanson & Knighton, 1996). At the channel scale, bifurcations and confluences play the role of basic unit processes of multithread systems. Understanding their own distinct morphology, flow structure and dynamics, as well as their mutual interplay, is therefore of crucial importance for managing water resources, mitigating the impacts of anthropic pressure [e.g., dams construction (Graf, 2006; Tong-Huan et al., 2020)], ensuring flood protection and adopting river restoration measures suitable for recovering deteriorated ecosystems (e.g., Habersack & Piégay, 2007; Wohl et al., 2015).

Almost all studies performed to date consider the two processes separately, although they frequently appear as closely interconnected. Figure 1 shows some illustrative examples of the morphological bond between bifurcations and confluences in different fluvial environments. Braided rivers like the Rakaia River in New Zealand (Figure 1a) are characterized by a complex, highly dynamic planform, where the water and sediment fluxes divide among multiple channels, although just few of them are morphologically active at a given time (Ashmore, 2001; Bertoldi et al., 2009a). In these fluvial systems, sequences of confluence-bifurcation units are ubiquitous features that control channel morphology and the spatial/temporal patterns of sediment transport (Ashmore, 2001; Ashworth, 1996). Midchannels bars and vegetated islands frequently recur in natural meandering rivers (Figure 1b), often associated with width fluctuations or chute and neck cutoff (Grenfell et al., 2012; Zolezzi et al., 2012). They also serve as key elements in the restoration of pristine multithread patterns, as in the case of the Drau River in Austria (Figure 1c), where a former side-channel was reopened with the aim of improving the habitat conditions, stabilize the river bed, and ensure flood protection through channel widening (Formann et al., 2007; Habersack & Piégay, 2007). A further example

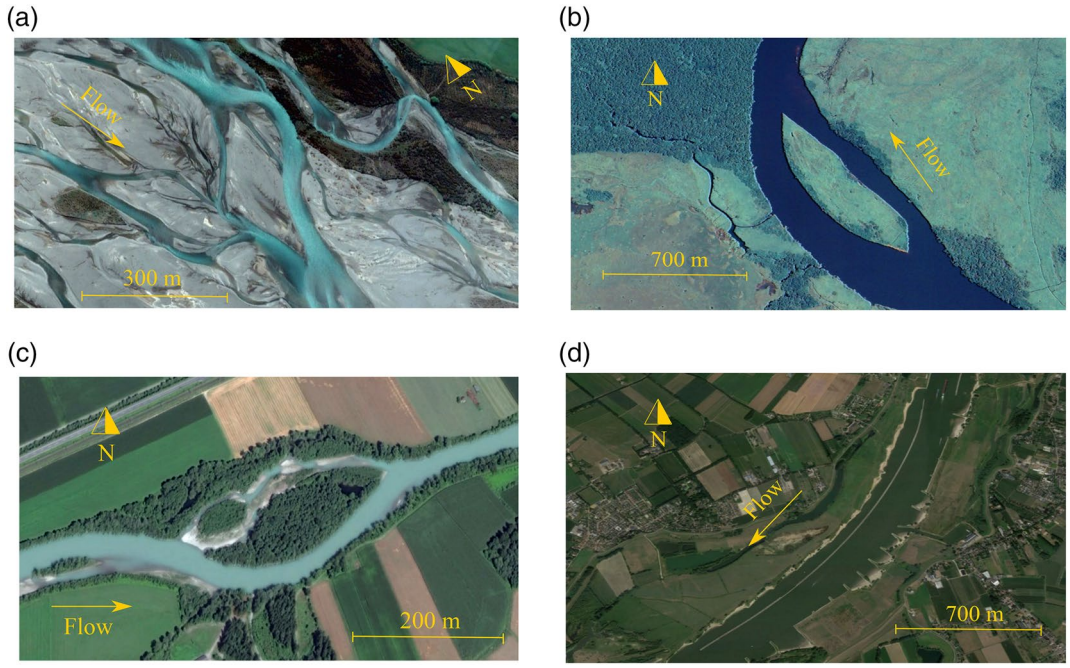


**Figure 1.** Satellite images showing different examples of bifurcation-confluence loops: (a) braided section of Rakaia River (New Zealand) 43°40′S, 171°53′E; (b) alluvial island on a tributary of Congo River (Central African Republic) 2°49′S, 18°20′E; (c) restored reach on the Drau River (Austria) 46°45′N, 13°19′E; (d) longitudinal training dam on the Waal River (Netherlands) 51°50′N, 5°24′E. From Google Earth, Digital Globe (2020).

comes from a novel interest of river restoration practices, namely the construction of the so-called longitudinal training dams to mitigate the effects of shipping on riverine habitat biodiversity and functionality and, at the same time, guarantee the fluvial navigation (Collas et al., 2018; de Ruijsscher et al., 2020) (Figure 1d).

In this work, we tackle the problem of analyzing the coupled morphodynamical response of such bifurcation-confluence systems. We therefore consider a simple "channel loop," where a single-thread channel divides into two secondary anabranches that reconnect further downstream, and we try to identify, within the framework of a simplified quasi two-dimensional approach, the key parameters that rule the mutual interplay between the upstream and downstream nodes.

River bifurcations often display an unbalanced distribution of water and sediment fluxes, with the two anabranches showing significant differences in their width and bed elevation (Zolezzi et al., 2006). This behavior has been highlighted by a large number of theoretical studies (Bolla Pittaluga et al., 2003, 2015; Redolfi et al., 2019; Salter et al., 2018; Wang et al., 1995), field observations (e.g., Zolezzi et al., 2006), numerical (Miori et al., 2012; Siviglia et al., 2013), and laboratory-scale physical models (Bertoldi & Tubino, 2007; Bertoldi et al., 2009b; Federici & Paola, 2003). These studies provide clear evidence on the existence of an inherent (free) instability mechanism that drives such unbalanced configuration. Most of the above analysis place emphasis on the bifurcation node and treat the downstream boundary condition as independently fixed. Therefore, they often simply assume a constant water level at the downstream end of the bifurcating channels, which implies that in the long term there are not slope differences that may advantage one of the two channels. In other words, they assume that the bifurcating system is "upstream controlled." This approach is also typically adopted for modeling channel networks (e.g., Kleinhans et al., 2012), side-channel systems (van Denderen et al., 2018), and channel loops (Bolla Pittaluga et al., 2003), where bifurcations are followed by confluences. However, bifurcation stability can be highly influenced by the downstream conditions, as clearly shown by recent analysis (Ragno et al., 2020; Salter et al., 2019, 2018). Specifically, the stability of a bifurcation is found to be very sensitive to a small water slope advantage of one of the two anabranches. Therefore, the assumption of water level constancy at a channel confluence (e.g., van Denderen et al., 2018) may be inadequate to analyze the morphodynamics of bifurcation-confluence loops, as

it ignores the feedback mechanism on the bifurcation driven by backwater effects induced by variations of the downstream condition.

Comparatively, fluvial confluences have been widely investigated in the last 40 years through physically scaled laboratory experiments, field investigations, numerical simulations, and conceptual models (e.g., Ashmore & Parker, 1983; Ashmore et al., 1992; Best, 1986, 1988; Best & Rhoads, 2008; Mosley, 1976; Paola, 1997). These studies have been mainly focused on studying their "local" hydrodynamics and morphodynamics, in order to analyze flow structures, bed morphology (e.g., scour depth) and sediment transport. However, much less research has been devoted to investigating the effect of the confluence on the upstream water and bed levels. Specifically, there are currently no theoretical models able to predict the upstream effect exerted by a confluence node when the bed is erodible.

In order to fill this gap and explore possible feedback mechanisms in bifurcation-confluence loops, in this work, we pursue the following objectives:

1. formulate a physically based model that is able to predict variations of the water surface elevation in mobile bed confluences
2. analyze whether the presence of a downstream confluence has an effect on the stability of the upstream bifurcation
3. identify the key parameters that control the stability of the coupled bifurcation-confluence system

To achieve the above aims, we first develop a novel theoretical model for an erodible-bed confluence, and subsequently we couple it with the bifurcation model proposed by Bolla Pittaluga et al. (2003). After a brief review on the state of the art of fluvial bifurcations (Section 2), the formulation of the confluence model is introduced in Section 3. The outcomes of the model are reported in Section 4. In Section 5, the governing equations of the coupled problem are analyzed by means of a linearization procedure. We then discuss the main implications of our results in Section 6, while Section 7 is devoted to some concluding remarks.

## 2. Background

Channel bifurcations show an intrinsic tendency to evolve toward unbalanced states. Specifically, even a geometrically symmetric bifurcation can spontaneously produce an uneven distribution of flow and sediment discharge in downstream anabranches because of an instability mechanism, which manifests itself with the formation of an upstream steady bar that deviates water and sediment fluxes toward the dominating branch (e.g., Edmonds & Slingerland, 2008; Le et al., 2018; Salter et al., 2019). As shown by Redolfi et al. (2016) such morphodynamical requirement sets an intriguing bond between the stability of bifurcations and the phenomenon of 2-D morphodynamic influence (Zolezzi & Seminara, 2001).

Bifurcation instability arises from an imbalance between the sediment distributed by the bifurcation and the transport capacity of the downstream branches (e.g., Bolla Pittaluga et al., 2003; Wang et al., 1995). In bedload-dominated rivers, this mechanism can be compensated by the gravitational effect of lateral bed slope on the sediment transport, which is more effective when the width-to-depth ratio is small. For this reason, the unbalanced configuration is observed to occur at relatively high values of the width-to-depth ratio (e.g., Bertoldi & Tubino, 2007; Bolla Pittaluga et al., 2015; Redolfi et al., 2019). These effects can be parsimoniously modeled following the approach of Bolla Pittaluga et al. (2003), who proposed to take into account the flow and sediment redistribution immediately upstream the bifurcation node by introducing a two-cell model, as sketched in Figure 2a. The length of the two cells, measured by the empirical parameter $\alpha$, physically represents the upstream extension of the effect of the bifurcation.

Water and sediment fluxes through the cells ($Q$ and $Qs$, see Figure 2b) are computed by considering the mass conservation equations, and assuming that the sediment flux is deflected with respect to the water flow by the action of gravity as follows:

$$\underbrace{\frac{Qs_y}{Qs_a}}_{\text{sediment flux direction}} = \underbrace{\frac{Q_y D_a}{Q_a D_{abc}}}_{\text{velocity direction}} - \underbrace{\frac{2r\alpha}{\sqrt{\theta_a}} \frac{\eta_b - \eta_c}{W_b + W_c}}_{\text{gravitational effect}}, \tag{1}$$

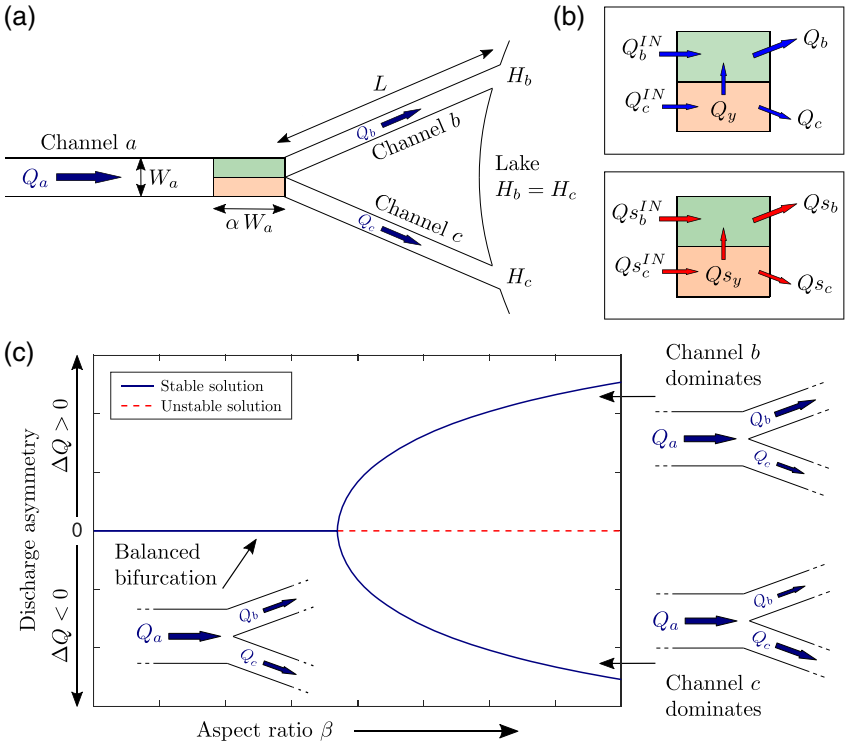


**Figure 2.** Schematization and example solution for a river bifurcation according to the Bolla Pittaluga et al. (2003) model. Panel (a) illustrates the symmetric planimetric configuration, with two bifurcates of equal length $L$ flowing into a lake that ensures an equal water surface elevation ($H_b = H_c$) at the downstream end of the channels. The topographic effect at the entrance of the bifurcation is accounted for by considering two cells of length $\alpha W_a$, which exchange water ($Q$) and sediment ($Qs$) fluxes as detailed in (b). Panel (c) shows the equilibrium solutions of the model, in terms of discharge asymmetry ($\Delta Q$) as a function of the channel aspect ratio ($\beta$): for $\beta$ larger than the critical threshold $\beta_C$ the balanced solution (dashed line) becomes unstable, and the system attains a stable state where one of the two bifurcates dominates (modified from Figure 2 of Redolfi et al. (2019)).

where $Q_y$ and $Qs_y$ are the water and sediment fluxes exchanged between the cells, $D_{abc}$ is the average depth, which can be taken equal to $D_a$ (Salter et al., 2018), $\theta_a$ is the Shields parameter of the upstream channel, $\eta_b$ and $\eta_c$ are the bed elevations at the inlet sections of the downstream channels. Finally $r$ is an empirical parameter that quantifies the effect of the lateral bed slope on the direction of the sediment transport (e.g., Baar et al., 2018; Ikeda et al., 1981). Equation 1 represents a simple, physically based nodal point relation, which can be conveniently incorporated into a one-dimensional model to describe the evolution of bifurcating channels. The set of nodal point conditions is then completed by assuming that at the bifurcation the water surface is nearly horizontal, which implies that the free surface elevation $H$ at the node is the same, both in the bifurcates and in the upstream channel.

An example of the equilibrium (steady state) solution is shown in Figure 2c in terms of the discharge asymmetry $\Delta Q$ (Bertoldi & Tubino, 2007):

$$\Delta Q := \frac{Q_b - Q_c}{Q_a}. \tag{2}$$

For low values of the aspect ratio of the inlet channel, $\beta_a = W_a/(2D_a)$, the bifurcation keeps stable and equally distributes water and sediment fluxes. The situation radically changes when $\beta_a$ exceeds a critical value, $\beta_C$, due to a "pitchfork bifurcation" of the equilibrium solution (Wiggins, 2003): the balanced configuration becomes unstable and the system evolves toward unbalanced equilibrium states, where one of the two branches carries most of the water and sediment flux. Results reported in Figure 2c refer to the symmetric configuration of Figure 2a, where channels are straight and the bifurcates have the same length $L$

and width $W$, and form the same angle with the incoming flow direction. Moreover, the bifurcating node is fed by constant and uniformly distributed water and sediment supply, while the downstream water level is constant and is the same for the two branches (i.e., $H_b = H_c$). In this case, the bifurcation is said to be "free," in as much as there are no external, "forcing" factors that may promote an unbalanced configuration (see Redolfi et al., 2019).

The critical value of the aspect ratio that discriminates between balanced and unbalanced configurations is found to depend primarily on the Shields parameter $\theta_a$ and, to a lesser extent, on the dimensionless Chézy coefficient $c_a$, defined as the ratio between the mean velocity and the friction velocity. Using the nodal conditions of Bolla Pittaluga et al. (2003) we obtain:

$$\beta_C = \mathcal{F}(\theta_a, c_a; r\alpha), \tag{3}$$

therefore, the estimated value of $\beta_C$ also depends on the choice of the coefficient $\alpha$. It is worth noting that the critical conditions for the stability of free bifurcations can also be found by means of the fully two-dimensional linear model proposed by Redolfi et al. (2016). Following this approach, the length of the upstream reach influenced by the bifurcation is a result of the model itself, so that no calibration of the coefficient $\alpha$ is needed. The analysis reveals that, consistently with the experimental observations of Bertoldi and Tubino (2007), the critical aspect ratio $\beta_C$ coincides with the resonant $\beta$-value that defines the threshold between prevailing downstream or upstream influence of 2-D morphodynamical changes.

### 2.1. The Role of the Downstream Boundary Condition

Various types of upstream and downstream effects can contribute to or counteract the response of the bifurcation depicted in Figure 2c (see Redolfi et al., 2019). Here, we are mainly concerned with downstream effects that can influence the bifurcation through variations of the energy slope, which in turn modify the flow rating curves and sediment transport capacity of the two bifurcates. In particular, water and sediment partition at the node depends on the slope asymmetry, defined as:

$$\Delta S := \frac{S_b - S_c}{S_b + S_c}. \tag{4}$$

Such slope asymmetry may derive from a variety of causes, such as a different length of the downstream channels (e.g., Kleinhans et al., 2008; Miori et al., 2006) or a nonidentical downstream boundary condition. In this paper, we focus on the second ingredient, while assuming the channel length to be the same (i.e., $L_b = L_c = L$). We note that at equilibrium a simple relation exists between the slope asymmetry and the difference of the downstream water surface elevations, namely:

$$\Delta S = -\frac{H_b - H_c}{2\bar{S}L}, \quad \bar{S} := \frac{S_b + S_c}{2}. \tag{5}$$

In their original formulation, Bolla Pittaluga et al. (2003) considered identical downstream boundary conditions (i.e., $H_b - H_c = 0$), which did not produce any slope asymmetry. A simple extension of this basic case can be obtained by considering a fixed, "externally imposed" value of $H_b - H_c$. In this case, the downstream condition breaks the symmetry of the system by introducing a preferential direction for flow and sediment fluxes, and the bifurcation is said to be "forced." Conversely, in the case of a channel loop the water surface elevation at the downstream end of the anabranches, where they reconnect at the confluence node, is not fixed a priori, because it depends on the amount of water and sediment delivered by the channels. Therefore, the downstream condition can be written in the general form:

$$H_b - H_c = \mathcal{F}(\Delta Q, \Delta Qs), \quad \Delta Qs := \frac{Qs_b - Qs_c}{Qs_a}. \tag{6}$$

Equation 6 sets a fascinating feedback mechanism, in as much as downstream variations of water surface elevation depend on the evolution of the bifurcation, which in turns is affected by downstream conditions through variations of the slope advantage. It is worth noticing that such mutual interplay has been recently

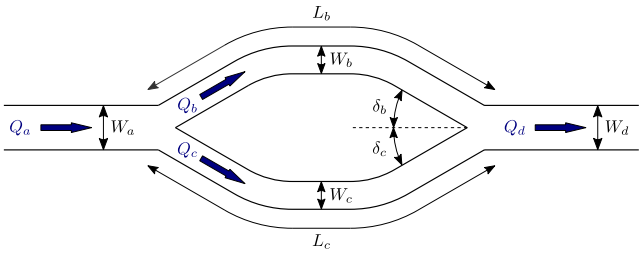


**Figure 3.** Planform configuration of the bifurcation-confluence loop, where the upstream channel $a$ splits in two branches $b$ and $c$ that then reconnect into a downstream channel $d$. Blue arrows denote the water discharge in each channel.

explored in the context of depositional systems by Salter et al. (2018), who considered a downstream condition in the form of a differential equation to account for bed aggradation induced by the incoming sediment flux. Their results suggest that the bifurcate that carries more water displays a higher downstream water surface elevation and therefore a negative gradient advantage, leading to an increased stability of the system (see their Figure 3).

## 3. Formulation of the Problem

In this analysis, we refer to the bifurcation-confluence loop illustrated in Figure 3. We assume that the banks are fixed, so that the planform geometry does not change in time. We formulate the model by considering a generic configuration, where the channel widths ($W_a$, $W_b$, $W_c$, $W_d$), the confluence angles ($\delta_b$, $\delta_c$), and the length of the connecting branches ($L_b$, $L_c$) can be freely chosen. For modeling the response of the bifurcation, we rely on the above-described model of Bolla Pittaluga et al. (2003). Therefore, we do not need to add new ingredients with respect to the existing literature. Conversely, for the confluence node, we need to formulate a new model, which is described in the following subsection.

### 3.1. A Model for Mobile Bed Confluences

In this section, we formulate a one-dimensional model for mobile bed channel confluences, which allows for determining how the water surface elevation adjusts depending on the incoming water and sediment fluxes. The model is based on the momentum balance in the streamwise direction on two distinct control volumes, as originally proposed by Shabayek et al. (2002) for a fixed bed channel confluence. We extend this model to mobile bed confluences by including the effect of the pressure forces acting on the bed, as needed to close the momentum balance when the bed is not flat. To this aim, we also provide a rigorous demonstration of how the momentum equation can be applied to a curved control volume (see Appendix A).

Figure 4 illustrates the confluence geometry adopted in the present formulation, with two channels $b$ and $c$ with rectangular cross section, having width $W_b$ and $W_c$ and slope $S_b$ and $S_c$, respectively, merging in a downstream channel $d$ of width $W_d$ and slope $S_d$, and forming angles $\delta_b$ and $\delta_c$ with the downstream direction. Two control volumes $CV_b$ and $CV_c$ are defined in proximity of the node, whose downstream widths depend on the discharge asymmetry $\Delta Q$.

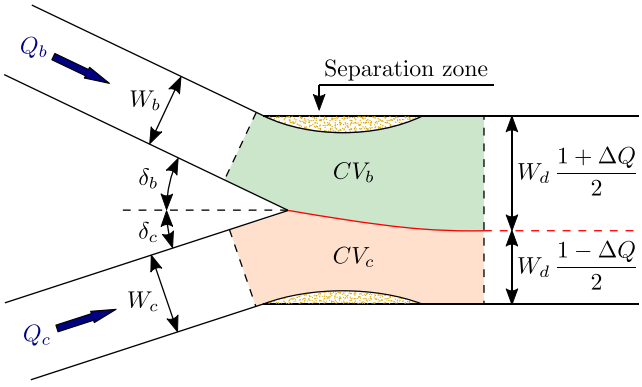


**Figure 4.** Schematic plan view of the confluence, illustrating the two control volumes and indicating the notation adopted for the formulation of the mathematical model. The downstream width of the control volumes is a function of discharge asymmetry. The red line denotes the shear layer between the two merging currents.

The sharp deviation of the flow at the confluence often induces the formation of a separation zone. This area, characterized by lower pressure, reduced velocity, and flow recirculation, represents a sort of "sediment trap," possibly leading to the formation of a bar within the postconfluence channel (Best, 1988; Leite Ribeiro et al., 2012). The width and length of the separation zone are found to increase with both the junction angle and the discharge asymmetry of the two incoming flows (Best & Reid, 1984; Hager, 1987).

The solid red line between the two control volumes in Figure 4 schematically represents the shear layer that develops along the interface between the two colliding streams, which is characterized by vortex generation and strong three-dimensionality of the flow structure (Best, 1986; Bradbrook et al., 2000; Rhoads & Sukhodolov, 2004). Another fundamental component of the flow structure at confluences is the presence of a double-helical circulation, characterized by two rotating cells that are converging at the stream surface and diverging near the bed (Biron & Lane, 2008). These cells drive the sediment toward the banks, forming a central scour whose depth and shape mainly depend on the discharge

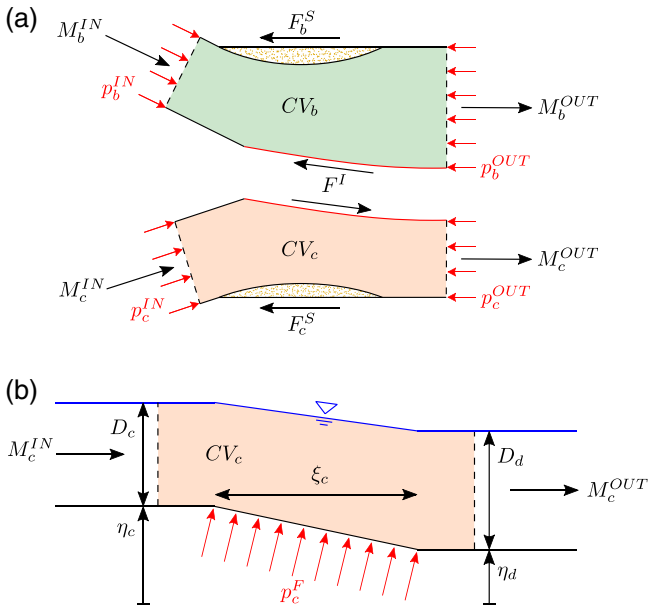


**Figure 5.** Illustration of the forces acting on the control volumes: (a) plan view, with the momentum terms ($M_{b,c}^{IN}$ and $M_{b,c}^{OUT}$) and pressure terms (red arrows) acting on the boundaries of the control volumes, the friction force due the presence of the separation zone around the junction corner ($F_{b,c}^S$), and the shear term along the mixing layer ($F^I$); (b) longitudinal section along the control volume $CV_c$, representing the pressure on the sloping bed ($p_c^F$).

asymmetry and the junction angle (Ashmore & Parker, 1983; Best, 1986; Mosley, 1976). The mechanism that leads to the formation of the helicoidal cells has been a widely discussed topic (e.g., Lane et al., 2000). Ashmore et al. (1992) attributed this phenomenon to the curvature of flow trajectories at the junction, which causes a secondary flow circulation due the imbalance between the centrifugal force and pressure gradient, while Paola (1997) suggested that the formation of helicoidal cells originates from the opposite components of momentum between the two colliding streams. Recently Sukhodolov and Sukhodolova (2019) verified the validity of the analogy to curved flows in open channels in a field-based study in the absence of a central scour.

The streamwise momentum conservation for the two control volumes $CV_b$ and $CV_c$ can be expressed as follows:

$$M_b^{OUT} - M_b^{IN} = P_b^{IN} - P_b^{OUT} + P_b^B + P_b^F - F^I - F_b^S, \tag{7a}$$

$$\underbrace{M_c^{OUT} - M_c^{IN}}_{\text{Momentum fluxes}} = \underbrace{P_c^{IN} - P_c^{OUT} + P_c^B + P_c^F}_{\text{Pressure forces}} + \underbrace{F^I - F_c^S}_{\text{Shear forces}}. \tag{7b}$$

The different forces acting on the two control volumes are sketched in Figure 5, while the formal structure and derivation of the streamwise momentum equation on a curved control volume are reported in Appendix A. Here, we consider a horizontal reference system, in which gravity does not appear in the streamwise momentum balance. Moreover, for the sake of simplicity, we neglect the frictional effects on the bottom and the lateral walls, as it is typically assumed when the control volume is short enough to make the "distributed" effects negligible. However, we notice that these components might be easily incorporated in the model by following the approach proposed by Shabayek et al. (2002).

The momentum fluxes on the left-hand side of Equations 7a and 7b are defined in the following form:

$$M_b^{IN} = \rho Q_b U_b, \quad M_b^{OUT} = \rho Q_b U_d, \tag{8a}$$

$$M_c^{IN} = \rho Q_c U_c, \quad M_c^{OUT} = \rho Q_c U_d, \tag{8b}$$

with $\rho$ indicating the water density, $U_b$ and $U_c$ the cross-sectionally averaged velocities.

The first terms on the right-hand side, $P_{b,c}^{IN,OUT}$, denote the hydrostatic forces due to water pressure acting at the upstream and downstream control sections of $CV_b$ and $CV_c$, which can be calculated as follows:

$$P_b^{IN} = \frac{1}{2}\gamma D_b^2 W_b, \quad P_b^{OUT} = \frac{1}{2}\gamma D_d^2 W_d \frac{1+\Delta Q}{2}, \tag{9a}$$

$$P_c^{IN} = \frac{1}{2}\gamma D_c^2 W_c, \quad P_c^{OUT} = \frac{1}{2}\gamma D_d^2 W_d \frac{1-\Delta Q}{2}, \tag{9b}$$

where $\gamma = \rho g$ is the specific weight of water.

Similarly, the terms $P_b^B$ and $P_c^B$, namely the longitudinal components of the pressure forces acting on the lateral boundaries, are expressed as:

$$P_b^B = \frac{1}{2}\gamma D_b^2\left[W_d\frac{1+\Delta Q}{2} - W_b\right], \tag{10a}$$

$$P_c^B = \frac{1}{2}\gamma D_c^2\left[W_d\frac{1-\Delta Q}{2} - W_c\right]. \tag{10b}$$

In natural confluences, the bed elevations at the outlets of the two confluent channels are typically different (Biron et al., 1996). As pointed out by Best and Roy (1991) this discordance is typically correlated with the formation of a bar at the mouth of the merging channels, with the presence of an avalanche face that descends upon a central scour. This morphological feature has been observed and investigated in field cases (Biron et al., 1993; Boyer et al., 2006; Leclair & Roy, 1997), numerical simulations (e.g., Bradbrook et al., 2001) and laboratory experiments (Best & Roy, 1991; Biron et al., 1996). In this case, the mixing process between the two incoming flows is affected by flow separation at the lee of the shallower channel. The mixing layer distortion, characterized by Kelvin-Helmholtz instability, leads to fluid upwelling from the deeper toward the shallower channel just downstream the separation zone (Best & Roy, 1991). Including such elevation difference is the key novel ingredient to incorporate into the model originally proposed by Shabayek et al. (2002) the morphological adjustment of the erodible bed. As illustrated in Figure 5b for the case of the control volume $CV_c$, this elevation difference can be modeled by considering a bed ramp of planimetric length $\xi_c$, with average slope $\overline{S}_c$ and planimetric area $A_c$:

$$\overline{S}_c = \frac{\eta_c - \eta_d}{\xi_c}, \quad A_c = W_d\frac{1-\Delta Q}{2}\xi_c, \tag{11}$$

which is subject to a quasi-hydrostatic pressure distribution:

$$p_c^F = \gamma\frac{D_c + D_d}{2}, \tag{12}$$

with the head given by the mean flow depth (Fraccarollo & Capart, 2002). The resulting pressure force can be readily calculated on the basis of Equation A9, which gives:

$$P_c^F = p_c^F\overline{S}_c A_c = \frac{1}{2}\gamma(\eta_c - \eta_d)(D_c + D_d)W_d\frac{1-\Delta Q}{2}, \tag{13}$$

where $(\eta_c - \eta_d)$ measures the bed elevation gap at the outlet of channel $c$ (see Figure 5b). We note that Equation 13 turns out to be independent of the length of the bed ramp, which implies that an identical solution could have been derived by considering a localized bed discontinuity (i.e., $\xi_c \to 0$). A similar procedure is adopted to compute the pressure force on the bed ramp for the control volume $CV_b$, which reads:

$$P_b^F = \frac{1}{2}\gamma(\eta_b - \eta_d)(D_b + D_d)W_d\frac{1+\Delta Q}{2}. \tag{14}$$

The last two terms of momentum balance Equations 7a and 7b represent the shear forces acting at the interface between $CV_b$ and $CV_c$, and those associated with the separation zones at the downstream corners of the confluence. These effects, whose detailed description would require the analysis of complex three-dimensional flow patterns, can be conveniently included in the present one-dimensional formulation using the simplified procedure proposed by Shabayek et al. (2002). The shear force along the interface between the two control volumes ($F^I$) is expressed as:

$$F^I = \tau^I A^I, \quad A^I = l^I D^I, \tag{15}$$

where $\tau^I$ is the average shear stress and $A^I$ is the area of the interface, given by the product of the relative length $l^I$ and depth $D^I$. The length of the interface $l^I$ is assumed to be proportional to the harmonic mean of the downstream widths of the two control volumes, an assumption based on the linear lateral growth rate of plane turbulent shear layers (Rajaratnam, 1976; Shabayek et al., 2002)

$$l^I \propto \frac{1}{2} W_d (1 - \Delta Q^2), \tag{16}$$

while the depth $D^I$ is set equal to the mean depth of the two merging channels. We therefore obtain the following expression for the shear force at the interface:

$$F^I = \frac{1}{2} \rho W_d K_I (U_b^2 - U_c^2)(D_b + D_c)(1 - \Delta Q^2), \tag{17}$$

where $K_I$ is a dimensionless interfacial shear coefficient.

Finally, the shear forces $F_b^S$ and $F_c^S$, originated by the formation of the separation zones at downstream corners of the confluence, are defined in the following form:

$$F_b^S = \frac{1}{2} \rho K_b U_b^2 D_b W_d (1 + \Delta Q), \tag{18a}$$

$$F_c^S = \frac{1}{2} \rho K_c U_c^2 D_c W_d (1 - \Delta Q), \tag{18b}$$

where $K_b$ and $K_c$ are dimensionless separation coefficients.

It is worth noting that the sum of the four pressure terms in the momentum balance (7), say $\Sigma P_c$ for the control volume $CV_c$, reduces to the following simple relationship:

$$\Sigma P_c = \frac{1}{2} \gamma (D_c + D_d)(H_c - H_d) W_d \frac{1 - \Delta Q}{2}. \tag{19}$$

Equation 19 reveals that the net effect of pressure terms is proportional to the difference of the water surface elevations $(H_c - H_d)$. We also notice that when both momentum fluxes and shear forces vanish (i.e., still water conditions), a horizontal free surface solution correctly satisfies the momentum balance.

The parameters $K_I$ and $K_{b,c}$ need to be calibrated on the basis of experimental data. In the present work we rely on the estimates proposed by Luo et al. (2018), which have been obtained from a linear regression of a set of available data, extending the original expressions proposed by Shabayek et al. (2002)

$$K_I = 0.21, \qquad K_{b,c} = 0.745 \delta_{b,c} - 0.1855, \tag{20}$$

where the angle $\delta_{b,c}$, expressed in radians, is measured over a length of $\mathcal{O}(W)$ at the intersection of the centerlines of the two channels. We note that Equation 20 is physically inconsistent for small angles, as it would give negative values of $K_{b,c}$ (i.e., the shear force would sustain the flow motion). We therefore impose a lower limit $K_{b,c} = 0$.

## 4. Results

To analyze the dynamics of a bifurcation-confluence loop, we refer to the simplest geometrical configuration. Specifically, we consider a symmetric planform geometry, where the connecting branches have the same length $L_b = L_c = L$, the same width $W_b = W_c = W_0/2$, and form the same angle at the confluence node $\delta_b = \delta_c = \delta$. Moreover, we consider that both the upstream and the downstream channels have twice the width of the connecting branches $W_a = W_d = W_0$. In the present analysis we take $r = 0.5$ and $\alpha = 4$ as typical reference values of the empirical parameters appearing in the nodal point condition (1) (Redolfi et al., 2016). We note explicitly that this choice does not affect the qualitative response of the system. Furthermore, we introduce the classical "Einstein scaling" to express the sediment flux:

$$Qs = W \sqrt{g \Delta d_{50}^3} \Phi(\theta, c), \quad \theta = \frac{U^2}{c^2 g \Delta d_{50}}, \tag{21}$$

where $\Delta$ is the relative submerged sediment density, $d_{50}$ is the median grain size, and $\Phi$ is the dimensionless transport function, for which we employ Parker (1990) formula for gravel bed channels and Engelund and Hansen (1967) relationship for sand bed channels. Finally, we compute the Chézy coefficient $c$ through the logarithmic friction formula (Keulegan, 1938):

$$c = 6 + 2.5 \log\left(\frac{D}{k_s}\right), \tag{22}$$

where $k_s$ is the Nikuradse equivalent roughness length. In the absence of dunes, this length can be assumed to be proportional to the median grain size (Engelund & Hansen, 1967), namely:

$$k_s = 2.5\, d_{50}. \tag{23}$$

A power-law expression for the Chézy coefficient as a function of $D/k_s$ (e.g., Wilkerson & Parker, 2011) would equally fit, without changing qualitatively the outcomes of the model.

We note that the flow conditions in each channel can also be described in terms of the Froude number, which is related to the other dimensionless parameters as follows:

$$Fr^2 = \theta c^2 \Delta \left(\frac{d_{50}}{D}\right). \tag{24}$$

When coupled with a closure relationship for friction, such as (22), Equation 24 provides a relation between the couples of dimensionless parameters ($\theta$, $c$) and ($\theta$, $Fr$), which can be therefore alternatively employed.

In equilibrium conditions, both water and sediment fluxes in channel $d$ coincide with those in channel $a$. For the simple, equal-width configuration examined, this implies that all the hydraulic parameters, including water depth, aspect ratio, Shields and Froude numbers are also equal. Therefore, in the following, we will employ the suffix $_0$ to denote generically the flow and sediment parameters in both upstream and downstream channels, when used as reference values in the analysis of model results.

This section is organized in two parts. We first apply our model to analyze the upstream effect of the confluence for varying flow conditions (Section 4.1). Then, we fully exploit the mutual interplay between bifurcation and confluence nodes and we analyze the equilibrium configurations of a channel loop (Section 4.2).

### 4.1. The Upstream Effect of a Confluence with Erodible Bed

The flow conditions at equilibrium, both in the main channel and in the tributary branches, are uniquely determined by means of the sediment and water continuity equations as a function of the dimensionless parameters $\beta_0$, $\theta_0$, $Fr_0$, and of the water and sediment discharge asymmetry ($\Delta Q$ and $\Delta Qs$, respectively). However, the parameters $\Delta Q$ and $\Delta Qs$ are usually covarying (i.e., the branch carrying more water also transports more sediment), and therefore we find more informative to adopt $\Delta Q$ and the slope asymmetry $\Delta S$ as independent parameters. This choice is fully equivalent, as $\Delta S$ and $\Delta Qs$ are clearly related.

In the following, we analyze the response of the confluence node to variations of the flow conditions in terms of two-dimensionless variables:

$$\Delta\eta := \frac{\eta_b - \eta_c}{D_0}, \qquad \Delta H := \frac{H_b - H_c}{D_0}, \tag{25}$$

which provide a measure of the asymmetry in bed elevation and water level at the outlet of the two incoming branches. Values of $\Delta\eta$ and $\Delta H$ can be readily computed from the momentum Equations 7a and 7b by considering $P_b^F$ and $P_c^F$ as unknowns, and then applying Equations 13 and 14 to compute $\eta_b$ and $\eta_c$.

In Figure 6a, the equilibrium solution for $\Delta\eta$ is shown as a function of the discharge asymmetry $\Delta Q$, for increasing values of downstream Froude number $Fr_0$. When $\Delta Q = 0$ (i.e., equal discharge in channel $b$ and $c$), the hydrodynamic conditions in the two branches are the same, and the confluence does not introduce

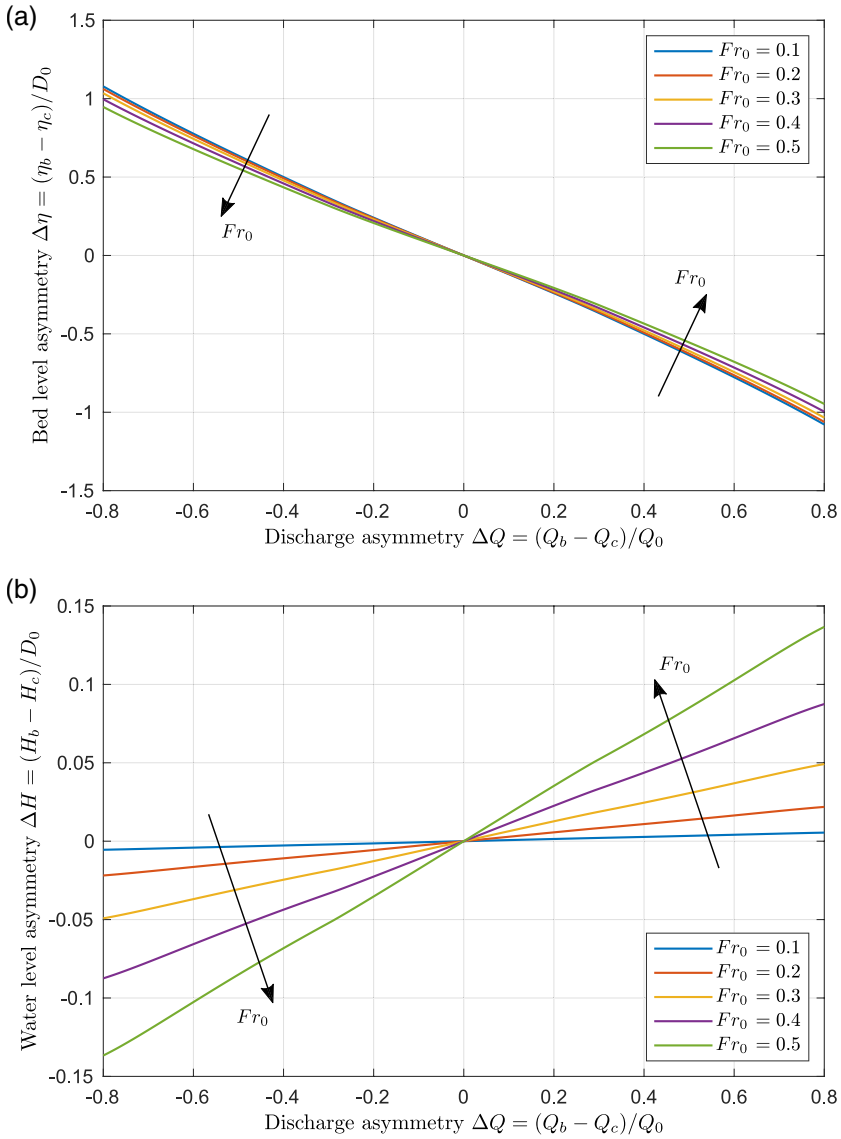


**Figure 6.** Response of the channel confluence to variations of the discharge asymmetry in terms of (a) bed level and (b) water level asymmetry, for different values of the Froude number ($Fr_0$) and zero slope asymmetry ($\Delta S = 0$). Differences in bed elevation are proportional to the square of the Froude number as outlined in Equation 26. Due to the symmetry of the geometrical configuration, both the plots show a point of symmetry with respect to the origin of the axes ($\Delta Q = 0$, $\Delta H = 0$).

any asymmetry in the water surface and bed elevation. The shear forces $F^S_{b,c}$ coincide for both control volumes, whereas $F^I$ is equal to zero (because $U_b = U_c$). In this condition, the confluence simply produces a difference between the upstream and the downstream bed elevation, which is induced by the energy dissipation at the separation zones (see Equation 28). When the incoming discharge partition is unequal, aggradation characterizes the branch that carries less discharge, leading to a higher value of the bed pressure force $P^F_{b,c}$, which is essential to maintain the momentum balance within the two control volumes. The resulting differences in the bed elevation between the two upstream branches are weakly affected by the Froude number, and gradually increase with the discharge asymmetry up to values comparable with the downstream water depth $D_0$.

From $\Delta\eta$ we can easily compute the water level asymmetry $\Delta H$, being $H = D + \eta$. As expected, when the Froude number vanishes ($Fr_0 \to 0$), i.e., when the momentum fluxes become negligible with respect to

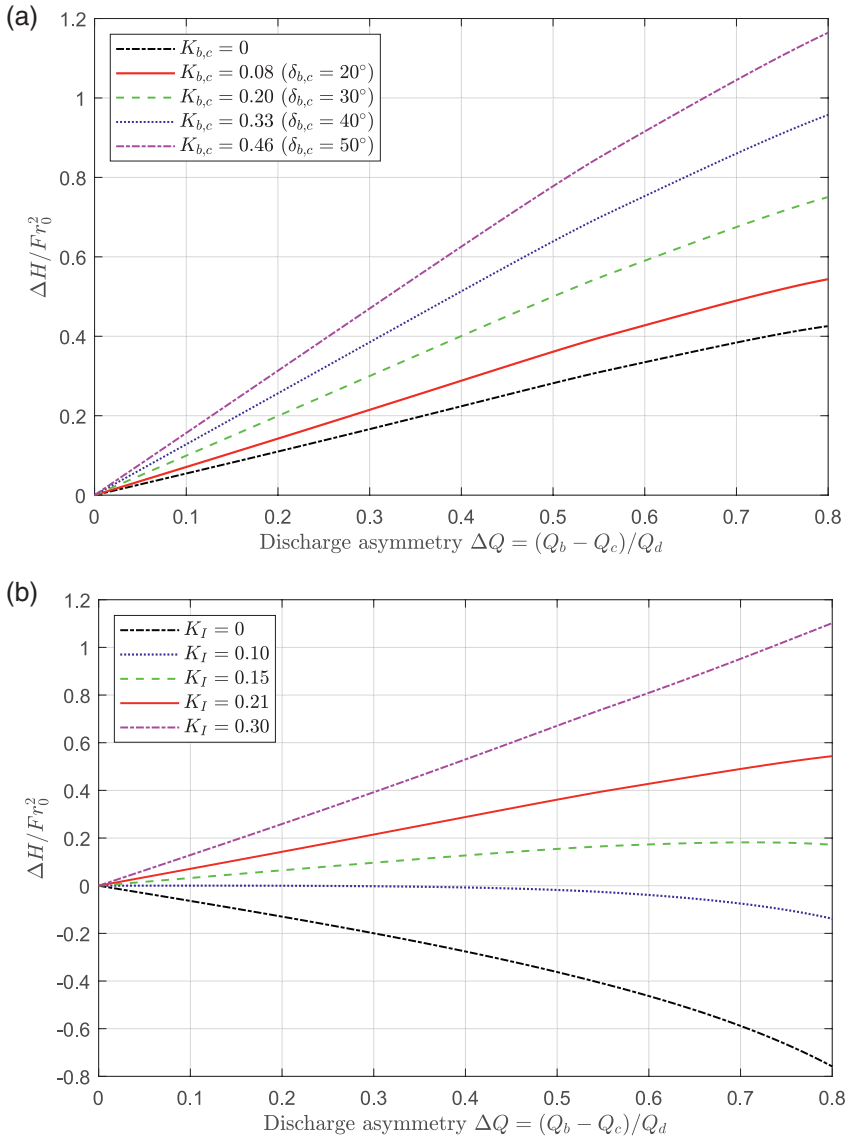


**Figure 7.** Sensitivity of the scaled water level asymmetry $\Delta H$ / $Fr_0^2$ to variations of the empirical parameters: (a) the separation coefficient $K_{b,c}$ and the associated confluence angle $\delta_{b,c}$ according to Equation 20; (b) the interfacial shear coefficient $K_I$. The solid red line indicates the value of both parameters adopted in the present analysis.

pressure forces, the water surface is nearly horizontal and therefore $\Delta H \to 0$. Conversely, by increasing the value of $Fr_0$ a distinct feature emerges: the branch that experiences the larger fraction of discharge shows a higher water surface elevation. Specifically, as illustrated in Figure 6b, the water level asymmetry displays a nearly linear growth with increasing discharge asymmetry. Moreover, $\Delta H$ turns out to be directly proportional to the square of the Froude number:

$$\Delta H \propto Fr_0^2. \tag{26}$$

In general, the resulting differences in water surface elevation are rather modest, being on the order of one-tenth of the water depth. For this reason, since the pioneering work of Taylor (1944) it is typically assumed that the water surface elevations of the two converging channels are equal (e.g., Gurram et al., 1997; Hsu et al., 1998). For most applications, this assumption can be fully accepted, as highlighted by several experimental and numerical studies (e.g., Coelho, 2015). However, as pointed out in Section 2.1, the sensitivi-

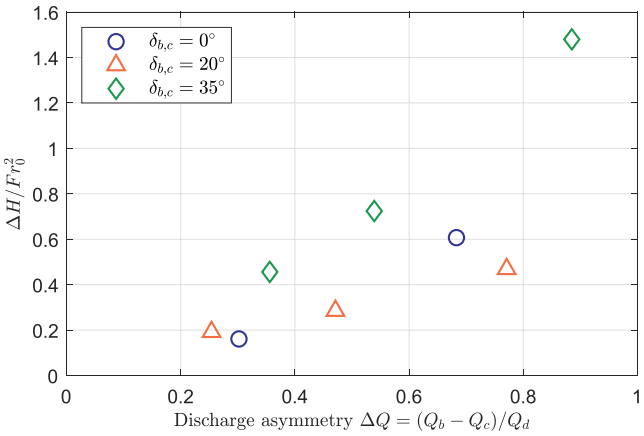


**Figure 8.** The values of the scaled water level asymmetry, $\Delta H \,/\, Fr_0^2$, as a function of discharge asymmetry $\Delta Q$, for three different values of the confluence angles $\delta_{b,c}$, as obtained from the field data of Sukhodolov and Sukhodolova (2019).

ty of bifurcations to variations of downstream conditions suggests that even narrow differences of the water surface elevation at the confluence node are likely to affect significantly the dynamic behavior of the whole system.

Results reported in Figure 6 are obtained by considering the Parker (1990) transport formula, and given values of the Shields parameter $\theta_0 = 0.08$, aspect ratio $\beta_0 = 20$ and junction angle $2\delta = 40°$. However, it is worth observing that model results are fully independent of the channel aspect ratio $\beta_0$, and negligibly affected by the Shields number $\theta_0$ and the choice of the sediment transport predictor. In particular, when the Engelund and Hansen (1967) transport formula is employed, results are exactly independent of the Shields parameter $\theta_0$. These observations highlight the primary importance of the Froude number $Fr_0$ in determining the dynamic response of the confluence.

Equation 26 suggests that the results can be conveniently analyzed in terms of the scaled water level asymmetry, $\Delta H \,/\, Fr_0^2$. In Figure 7, we perform a sensitivity analysis due to understand the importance of the two empirical parameters $K_I$ and $K_{b,c}$. Due to the symmetry properties highlighted earlier, we report only half of the plot. Figure 7a reveals that the scaled water level asymmetry increases with $K_{b,c}$. This can be explained by considering that the dissipative shear force at the separation zone, as given by Equation 18a, increases more at the side where discharge (and velocity) are higher, thus requiring a higher pressure force toward the dominant channel. Noteworthy, the water level asymmetry $\Delta H$ positively correlates with the discharge asymmetry $\Delta Q$ also when the coefficients $K_{b,c}$ vanish. According to Equation 20, this occurs when the junction angle is fairly small ($\delta_{b,c} \leq 14°$). However, this situation is probably more common in natural confluences, in which the separation zone may be often absent (Ashmore et al., 1992; Biron et al., 1993).

Similarly, in Figure 7b, we explore the role of different values of the interfacial shear coefficient, from the extreme case $K_I = 0$ (hence, neglecting the effect of the interfacial shear term in the momentum balance) to the more realistic values of 0.2–0.3 reported by Shabayek et al. (2002) and Luo et al. (2018) (see supporting information). This analysis reveals the fundamental role of the parameter $K_I$, as a value of at least 0.1 is needed to obtain the same qualitative behavior depicted in Figure 6, where the confluence tilts toward the dominant channel (i.e., that carrying more water and sediment).

The above findings are supported by the results of the recent field experiments of Sukhodolov and Sukhodolova (2019), who measured discharge, water depth, velocity, and free surface elevation, in a 10-m wide symmetric confluence with fixed, artificial banks but erodible bed, for three different confluence angles at different values of discharge asymmetry. We calculated $\Delta H$ on the basis of the contour maps reported in their Figure 6, by estimating the average water surface elevation in the two branches at the entrance of the confluence (i.e., at a distance of about 0.7–0.9 $W_0$ with respect to the confluence node). Results reported in Figure 8 highlight four remarkable characteristics of the confluence response to varying conditions: (i) the water surface level is always higher in the branch that carries most of the flow; (ii) the scaled water surface asymmetry $\Delta H \,/\, Fr_0^2$ increases with the discharge asymmetry, by following a roughly linear trend; (iii) the ratio $\Delta H \,/\, Fr_0^2$ tends to increase with the confluence angle, although no significant differences can be appreciated when comparing cases with $\delta_{b,c} = 0°$ and $\delta_{b,c} = 20°$; (iv) values of the scaled water level asymmetry corresponding to $\Delta Q \simeq 0.8$ are in the order of 0.6 for the two lower angles, and about 1.3 for $\delta_{b,c} = 35°$. The above results are not directly comparable with those reported in Figures 6 and 7, because the asymmetry of the energy slope in the experiments was not vanishing. Nevertheless, the experimental outcomes suggest that our approach based on a global momentum balance is able to capture the essential response of the confluence asymmetry to varying flow and geometrical conditions.

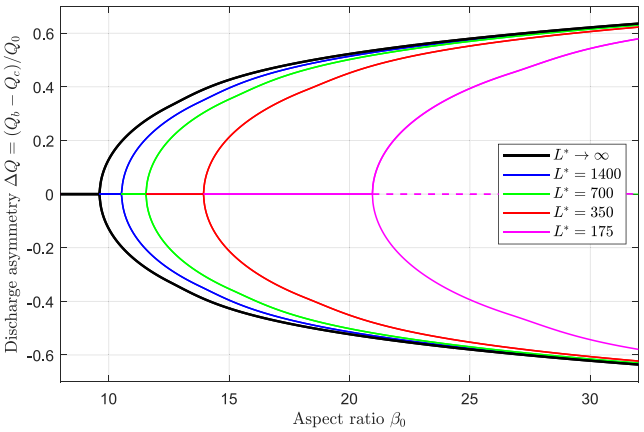


**Figure 9.** Equilibrium configurations of a bifurcation-confluence loop, plotted as a function of the discharge asymmetry, $\Delta Q$, and the aspect ratio of the main channels, $\beta_0$, for different values of the dimensionless length of the connecting channels ($L^* = L/D_0$). The dashed lines indicate unstable solutions. Example with $\theta_0 = 0.08$ and $c_0 = 12$. The critical aspect ratio, at which the unbalanced solutions ($\Delta Q \neq 0$) appear, increases significantly from the case of $L^* \to \infty$ to shorter connecting channels, which reveals the stabilizing effect of the confluence.

### 4.2. Equilibrium Configurations of the Bifurcation-Confluence Loop

On the basis of river bifurcation theory described in Section 2, and the confluence model formulated in Section 3, we now connect the two systems, exploring the morphodynamics of the bifurcation-confluence loop sketched in Figure 3. This is achieved by coupling the nodal point relation at the bifurcation (1) with the momentum balance at the confluence (7) by means of Equation 5, which relates the (downstream) water level differences with the (upstream) slope asymmetry at equilibrium. Differently from Section 4.1, we determine the reference flow conditions by setting the dimensionless parameters $\beta_0$, $\theta_0$, and $c_0$. The rational motivation behind this choice will be more clear after Section 5, keeping in mind the link between $c_0$ and Froude number $Fr_0$ expressed by Equation 24.

An example of the equilibrium diagram of a bifurcation-confluence loop is shown in Figure 9, where the equilibrium values of discharge asymmetry $\Delta Q$ are reported as a function of the aspect ratio $\beta_0$ and for different values of the scaled length $L^*$, defined as the ratio between the length of the bifurcates ($L$) and the reference water depth ($D_0$). When the connecting branches are infinitely long ($L^* \to \infty$), the presence of the confluence is not felt by the bifurcation, and the model gives exactly the same solution of the sole bifurcation problem as obtained by Bolla Pittaluga et al. (2003), which is reported in Figure 2. Conversely, gradually decreasing the anabranches length, the critical value of the aspect ratio at which the balanced solution ($\Delta Q = 0$) becomes unstable gets larger. This behavior is associated with the negative feedback exerted by the confluence on the upstream bifurcation, which increases the stability of the system. When the aspect ratio $\beta_0$ exceeds the critical value $\beta_C$, the geometric discontinuity that originates at the inlet of channels $b$ and $c$ steers a greater fraction of water and sediment fluxes to one of the two branches, promoting the development of an unbalanced configuration. In this case, the downstream confluence responds by increasing the water level of the dominant branch (Figure 6), therefore reducing its slope. This effect tends to re-equilibrate the bifurcation, so that the system has the possibility to maintain the balanced state for higher values of the aspect ratio $\beta_0$ with respect to the case of the sole bifurcation.

## 5. Linear Analysis of the Coupled System

To determine the marginal stability conditions and the associated critical parameters, we perform a linear analysis of the mathematical problem. When the system is in marginal stability conditions, small initial perturbations with respect to the equilibrium configuration neither grow nor decay in time. Therefore, in these conditions, a nontrivial steady solution of the linearized system exists. With reference to the diagrams of Figures 2 and 9, this occurs when the equilibrium solution shows a pitchfork bifurcation (i.e., when the channel aspect ratio equals the critical value $\beta_C$).

As a first step, the dependent variables of the problem can be expressed in dimensionless form as follows:

$$\left\{D^*,\eta^*,H^*,L^*\right\} = \frac{\left\{D,\eta,H,L\right\}}{D_0}, \quad q^* = \frac{Q\ /\ W}{Q_0\ /\ W_0}, \quad qs^* = \frac{Qs\ /\ W}{Qs_0\ /\ W_0}, \tag{27}$$

where $q$ and $qs$ indicate the water and sediment fluxes per unit width, and the superscript * denotes dimensionless quantities. We note explicitly that the outcomes of linear analysis do not depend on the choice of the adopted scaling length for $L$. The reason behind the choice of $D_0$ is clarified in Section 6.

Because of the symmetry of the geometrical configuration, the set of governing equations clearly admits a balanced solution, corresponding to everywhere-uniform flow conditions, where the bifurcation equally distributes water and sediment fluxes (i.e., $\Delta Q = \Delta Qs = 0$) and the confluence does not introduce any asymmetry (i.e., $\Delta H = 0$). In this condition, the confluence merely produces a difference between the upstream

and the downstream bed elevation (and an equal difference in the water surface elevation) induced by the energy dissipation at the separation zones. Specifically, the bed elevations at the confluence node depend on a balance between the friction force at the separation zone ($F^S_{b,c}$) and the pressure terms acting on the bottom ($P^F_{b,c}$), which gives the following relation:

$$\eta^*_b = \eta^*_c = \eta^*_d + Fr_0^2 K_b. \tag{28}$$

The linear analysis is performed by considering such balanced solution as a basic, reference state, which is then modified by adding a small perturbation. In particular, we expand a generic variable $X^*$ in the form:

$$X^* = X^*_0 + \epsilon X^*_1, \qquad \epsilon \ll 1, \tag{29}$$

where $X^*_0$ is the reference value and $\epsilon X^*_1$ represents the perturbation, with $\epsilon$ being a small parameter. Substituting from Equation 29 into the governing equations, expanding in Taylor series and neglecting the higher-order, $\mathcal{O}(\epsilon^2)$, terms arising from the nonlinear interactions, we obtain a set of linear algebraic equations. Application of the above procedure to the continuity of mass and sediment fluxes gives:

$$q^*_{b1} = -q^*_{c1}, \qquad qs^*_{b1} = -qs^*_{c1}, \tag{30}$$

which implies that the linear solution is fully antisymmetric, meaning that the variations of water depth, slope and water surface elevation are equal and opposite in the two secondary branches (e.g., $D^*_{b1} = -D^*_{c1}$). This allows us to analyze the solution for one side of the domain only, say the channel $b$, for which the following system of five linear equations in the five unknowns $(q^*_{b1}, qs^*_{b1}, D^*_{b1}, S_{b1}, H^*_{b1})$ is obtained:

$$\begin{cases} q^*_{b1} = \dfrac{1}{2}\dfrac{S_{b1}}{S_0} + \left(\dfrac{3}{2} + c_D\right) D^*_{b1}, \\ qs^*_{b1} = \left(\Phi_T + \Phi_D\right) D^*_{b1} + \Phi_T \dfrac{S_{b1}}{S_0}, \\ qs^*_{b1} = q^*_{b1} + \dfrac{4r\alpha}{\beta_0\sqrt{\theta_0}} D^*_{b1}, \\ H^*_{b1} = Fr_0^2 \left[\zeta\, q^*_{b1} + (K_b\ /\ 2 - \zeta) D^*_{b1}\right], \\ \dfrac{S_{b1}}{S_0} = -\dfrac{H^*_{b1}}{S_0 L^*}, \end{cases} \tag{31}$$

where the parameter $\zeta$ is defined as:

$$\zeta := 8K_I + 2K_b - 1, \tag{32}$$

and the coefficients $c_D$, $\Phi_D$, and $\Phi_T$, which measure the sensitivity of the Chézy coefficient and the sediment flux to variations of water depth and Shields parameter, read:

$$c_D := \frac{D_0}{c_0}\frac{\partial c}{\partial D}\bigg|_{D_0}, \quad \Phi_D := \frac{D_0}{qs_0}\frac{\partial qs}{\partial D}\bigg|_{D_0}, \quad \Phi_T := \frac{\theta_0}{qs_0}\frac{\partial qs}{\partial \theta}\bigg|_{\theta_0}. \tag{33}$$

The mathematical expression of the coefficients depends on the friction and the transport formula adopted (see Redolfi et al., 2019).

The first two equations of system (31) represent the flow and sediment rating curves. The third equation is the nodal relation proposed by Bolla Pittaluga et al. (2003). The fourth equation is the linearized momentum balance applied to the control volume $CV_b$ at the confluence, as formulated in Equation 7a. The last equation defines the relationship between the channel slope and the downstream water levels, which is directly obtained from Equation 5.

The linear system (31) admits a trivial solution, characterized by vanishing perturbations. However, when its determinant is zero, a nontrivial solution is also possible. This allows for determining the marginal conditions for the stability of the bifurcation-confluence loop, which can be generically expressed by means of the following functional relationship:

$$\mathcal{F}\left(\mathcal{R},\Lambda,\theta_0,c_0,K_b,K_I\right)=0, \tag{34}$$

where

$$\mathcal{R}:=\frac{r\alpha}{\beta_0\sqrt{\theta_0}},\quad \Lambda:=\frac{Fr_0^2}{S_0L^*}. \tag{35}$$

Equation 34 allows for calculating the critical values of the relevant parameters. Specifically, the analytical expression for the critical value of the aspect ratio $\beta_C$ takes the following form:

$$\beta_C=\frac{2r\alpha}{\sqrt{\theta_0}}\frac{2+\Lambda\zeta}{\Phi_T+\Phi_D-c_D-3/2+\Lambda\varphi}, \tag{36}$$

where:

$$\varphi:=\zeta\left[\frac{\Phi_T+\Phi_D}{2}-\Phi_T(3/2+c_D)\right]-\left(K_b/2-\zeta\right)(\Phi_T-1/2). \tag{37}$$

In general, the critical aspect ratio $\beta_C$ depends on the Shields parameter $\theta_0$ and the scaled channel length $L^*$, as illustrated in Figure 10 for the case of gravel (panels a–c) and sand bed channels (panels b–d). When the anabranches are infinitely long, the parameter $\Lambda$ vanishes, and Equation 36 reduces to the form of the sole bifurcation (Bolla Pittaluga et al., 2015; Redolfi et al., 2019). This gives the results illustrated in Figures 10a and 10b, which display the well-known, opposite trend with the Shields parameter for the gravel and the sand bed cases (Bolla Pittaluga et al., 2015; Edmonds & Slingerland, 2008). Conversely, as the length of the connecting channels gets shorter the critical aspect ratio increases, regardless the flow conditions and both in the gravel and in the sand bed case. This highlights the stabilizing role exerted by the downstream confluence, whose effect inversely depends on the dimensionless length $L^*$ and ultimately leads to very high values of $\beta_C$. The response of the channel loop to variations of the channel length appears more evident in Figures 10c and 10d, which show that the critical aspect ratio invariably tends to infinite when the connecting branches are sufficiently short. As a result, the linear response is characterized by the presence of two asymptotes, both in the gravel and the sand case: the horizontal asymptote coincides with $\beta_C^\infty$ (i.e., the solution of Bolla Pittaluga et al. (2003)), while the vertical asymptote corresponds to the value of the scaled anabranches length ($L^*$) that makes the system invariably stable, independently of the aspect ratio.

Figures 10c and 10d also reveal that the two parameters $L^*$ and $\beta_0$ are equally important in determining the stability of the channel loop. This suggests the opportunity to define a critical value of the anabranches length, $L_C^*$, as a function of the aspect ratio and the Shields number. An analytical expression for this critical length can be readily derived from Equation 34, which gives:

$$L_C^*=c_0^2\frac{\varphi+2\mathcal{R}\zeta}{\Phi_T+\Phi_D-c_D-3/2-4\mathcal{R}}. \tag{38}$$

## 6. Discussion

This work represents the first attempt to include within a unified theoretical framework the morphodynamic response of river bifurcations and confluences. This has been done by considering the state of the art of theoretical models for both bifurcations and confluences, which are coupled together to analyze the global dynamics of the system. Specifically, we have followed a quasi-2D approach, where the complex, highly three-dimensional flow and sediment transport pattern at the nodes are modeled by considering couples

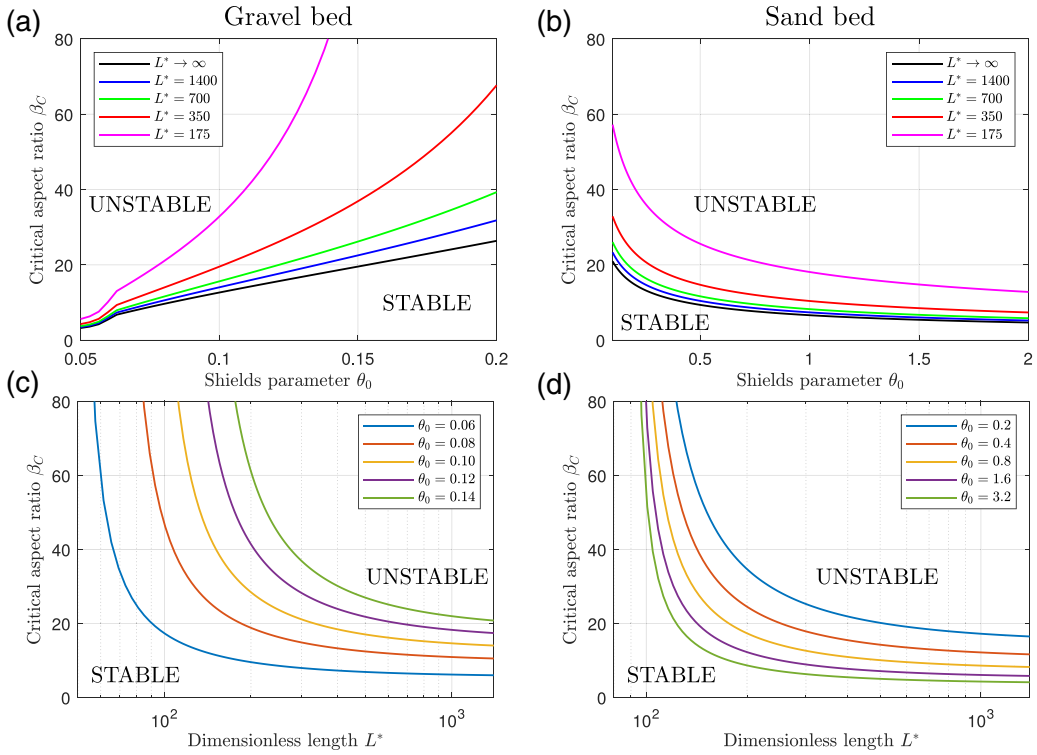


**Figure 10.** The critical aspect ratio $\beta_C$ as a function of the Shields parameter $\theta_0$ and of the scaled length $L^*$. Values for gravel bed (left panels) and sand bed (right panels) channels are obtained by employing the Parker (1990) and Engelund and Hansen (1967) transport formula, respectively, and $c_0 = 12$. When $\beta_0 < \beta_C$ the balanced configuration keeps stable, while for $\beta_0 > \beta_C$ the system becomes unstable, leading to an unbalanced distribution of water and sediment fluxes. The black line in panels (a) and (b) indicates the critical aspect ratio for the sole bifurcation ($\beta_C^\infty$).

of cells (or control volumes) that can exchange mass and momentum fluxes. A key novelty of this work is represented by our confluence model. Starting from the approach proposed by Shabayek et al. (2002), we have provided a sound formulation of the streamwise momentum balance on a curved control volume (see Appendix A), and introduced an additional term representing the pressure force acting on the sloping bottom, which results from the morphological adjustments of the mobile bed.

### 6.1. The Stabilizing Effect of the Confluence

The present work indicates that water level variations at a fluvial confluence affect the stability and the evolution of an upstream bifurcation. In particular, when the distance between the two nodes is sufficiently short, the effect of the confluence contributes to maintain a stable balanced configuration, where the flow is equally partitioned in the downstream branches. This effect is clearly related to the fact that the confluence tends to increase the water elevation of the channel that is carrying the higher discharge fraction. This causes a decrease of the slope of the dominating branch, which acts as a negative feedback that tends to re-establish a balanced distribution of water and sediment fluxes.

### 6.2. Key Controls on the Dynamic of the System

As highlighted earlier, the stability of the bifurcation-confluence loop essentially depends on the two following parameters:

$$\underbrace{\mathcal{R} = \frac{r\alpha}{\beta_0\sqrt{\theta_0}}}_{\text{Bifurcation parameter}}, \qquad \underbrace{\Lambda = \frac{Fr_0^2}{S_0 L^*}}_{\text{Confluence parameter}} \tag{39}$$

The parameter $\mathcal{R}$ is fundamental in determining the dynamics of the bifurcation (Bolla Pittaluga et al., 2003, 2015), as it essentially defines the capacity of the gravitational pull to deviate the sediment flux. This effect is inversely proportional to the channel aspect ratio $\beta_0$, which therefore assumes a primary role in determining the stability of bifurcations. Conversely, the parameter $\Lambda$ defines the effect of the confluence on the stability of the loop, and can be interpreted as a measure of the slope asymmetry potentially generated by the confluence. Specifically, considering the definition of $\Delta H$ (25), its dependence on the square of the Froude number (26), and the equality $\overline{S} = S_0$ near the marginal stability conditions, Equation 5 gives:

$$\Delta S = \frac{D_0 \Delta H}{2\overline{S}L} \propto \frac{D_0 Fr_0^2}{S_0 L} = \Lambda, \tag{40}$$

which shows the close relationship between $\Lambda$ and the slope asymmetry $\Delta S$. It is also worth noticing that the Froude number typically tends to covary with the slope, as mathematically expressed by the relation:

$$\frac{Fr_0^2}{S_0} = c_0^2, \tag{41}$$

where $c_0$ is weakly sensitive to variations of the channel slope, showing average values of about 10–12 in both gravel bed and sand bed rivers (see Parker et al., 2007; Wilkerson & Parker, 2011). Substituting from Equation 41 into 39 we then obtain:

$$\Lambda = \frac{c_0^2 D_0}{L}. \tag{42}$$

Equation 42 suggests that the correct scale for the channel length is given by the product $c_0^2 D_0$. This represents an important result of our analysis, because it marks a clear difference with respect to the classic scaling based on the backwater length, defined as the ratio between the water depth $D_0$ and channel slope $S_0$ (e.g., Paola & Mohrig, 1996), which represents the typical length scale of backwater effects in fluvial and deltaic systems. For example, the backwater length determines the extent of the propagation of tidal currents into rivers (e.g., Ragno et al., 2020; Seminara et al., 2012), the length of upstream flow profiles generated by instream structures (e.g., Samuels, 1989), and it has been employed for studying deltaic avulsions (e.g., Chadwick et al., 2019; Moodie et al., 2019). In these cases, the effect of the channel slope is clear, as a given elevation difference (say $\Delta H = 0.1$ m) can be felt nearly 10 times further upstream when $S$ reduces, e.g., from 1% to 0.1%.

A similar effect also occurs in bifurcation-confluences loops, in which, when slope decreases, the bifurcation is potentially more sensitive to variations of the downstream boundary conditions. However, the variations of the water surface elevation produced by the confluence, being proportional to $Fr_0^2$, also reduce for lower slopes, and these two effects tend to compensate. For the same reason, but from an opposite point of view, when Froude number is small, the water surface asymmetry at the confluence node is nearly vanishing. In these conditions, it seems reasonable to assume that the water surface level is the same in the two branches (e.g., Kleinhans et al., 2012; Schaffranek et al., 1981). Nevertheless, the low channel slope associated with the small value of the Froude number makes the bifurcation more sensitive to downstream effects, so that even small variations of the confluence level are sufficient to cause a significant effect on the water and sediment distribution. The independence of the loop solution from the Froude number also implies that, once the Chézy coefficient $c_0$ and the Shields number $\theta_0$ are fixed, calculation of the grain size from Equation 23 is not needed. This suggests that the above results are also valid in the case of dune-covered channels, provided suitable sediment transport relations are chosen.

The stability diagram of the bifurcation-confluence loop becomes more clear and significant when represented in terms of the two key parameters (39), as reported in Figure 11, for several reasons. First, it does not show singularities: the asymptotic behavior appearing in Figures 10b and 10c does indeed depend on the

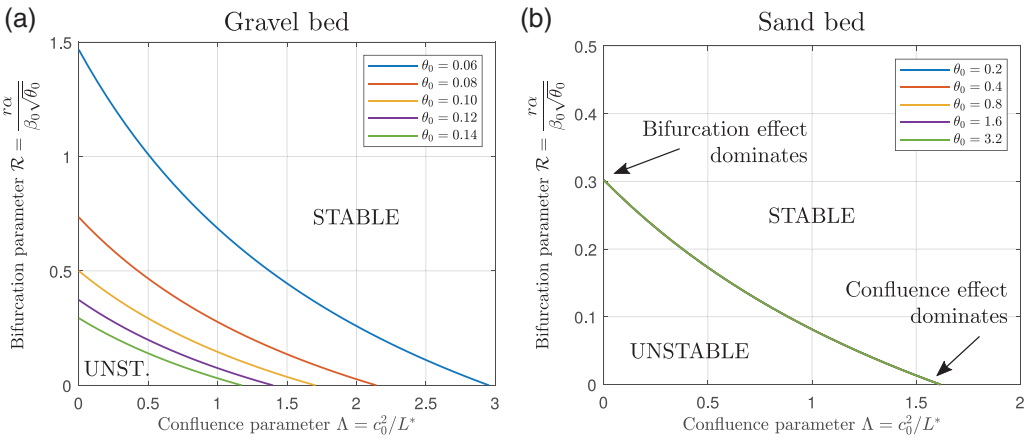


**Figure 11.** Stability diagram for the bifurcation-confluence loop, plotted as a function of the key controlling parameters $\mathcal{R}$ and $\Lambda$ for (a) gravel bed and (b) sand bed channels. The regions where $\Lambda$ or $\mathcal{R}$ vanish represent the conditions where the stability of the system is dominated by the "bifurcation effect" (i.e., the effect of the gravitational pull on the sediment transport at the bifurcation node) or by the "confluence effect" (i.e., the negative feedback exerted by the confluence through variations of the slope asymmetry), respectively.

fact that the parameters $\beta_0$ and $L^*$ appear at the denominator of Equation 39, so that conditions where the marginal stability curve approaches $\Lambda = 0$ (i.e., dominating "bifurcation effect") or $\mathcal{R} = 0$ (i.e., dominating "confluence effect") are attained for values of the critical parameters $L_C^*$ and $\beta_C$ that tend to infinity. Second, it is independent of the empirical parameters $r$ and $\alpha$, as their effect is fully incorporated in the definition of the key controlling parameters (39). Third, it includes part of the effect of the Shields number and the Chézy coefficient. Specifically, the residual effect of $c_0$ is very weak, to the point that it exactly vanishes when adopting a friction formula having the form of a power-law (e.g., the Manning formula). Similarly, there is no residual effect of the Shields number when considering sand bed cases, where the transport rate is given by the power-law transport formula of Engelund and Hansen (1967), while a rather important effect remains in gravel bed cases. This is clear from Figure 11a, which shows that the region of instability narrows when increasing the Shields number, consistently with existing theoretical models for gravel bed bifurcations (Bolla Pittaluga et al., 2003; Redolfi et al., 2016).

We note that the present model is based on the commonly adopted assumption that the water level at the bifurcation node is the same in the two branches. This was originally introduced by Bolla Pittaluga et al. (2003) by assuming the conservation of energy across the bifurcation and neglecting the kinetic terms, which is strictly valid only at low Froude numbers. However, the reason behind this assumption is more profound, and therefore, the uniformity of water levels is more generally legitimated in this case, as the presence of a large-scale, upstream steady bar generated by the bifurcation (Bertoldi & Tubino, 2007; Redolfi et al., 2016) allows the flow to gradually adapt to the bottom topography without significant deformations of the free surface, even at moderate Froude numbers. Specifically, calculations based on the steady bar model of Zolezzi and Seminara (2001) reveal that differences in the water surface elevation are at least 1 order of magnitude smaller than those reported in Figure 6b, independently of the Froude number.

### 6.3. Implication for Suspension-Dominated Systems

In sand bed channels, the sediment transport is often dominated by the presence of suspended load. As suggested by several authors (e.g., Kleinhans et al., 2008; Redolfi et al., 2019), suspended load is substantially not deflected by the gravitational pull, which makes bifurcations more unstable. Specifically, in the limiting case where the gravitational effect is negligible (i.e., $r = 0$, $\mathcal{R} = 0$), the sediment flux is distributed proportionally to the water discharge, and the sole bifurcation turns out to be invariably unstable, also consistently with the classic analysis of Wang et al. (1995). Nonetheless, bifurcations in sand bed rivers are often observed to be stable over an extended period of time. This contradiction may be at least partially explained by considering that the presence of the confluence induces a distinct stabilizing effect, fully independent

**Table 1**
*Relevant Dimensionless Parameters for Different Bifurcation-Confluence Loops in Natural Settings (Renous River, Canada, See Burge, 2006), and Resulting From an Artificial River Restoration Measure (Drau River, Austria, See Formann et al., 2007)*

| River | Case | $\beta_0$ | $\theta_0$ | $c_0$ | $Fr_0$ | $L/D_0$ | $\alpha$ | $\mathcal{R}$ | $\Lambda$ | $\beta_C^\infty$ | $\beta_C$ |
|---|---|---|---|---|---|---|---|---|---|---|---|
| Renous | Bif. 2 | 17.0 | 0.035 | 11.3 | 0.58 | 167 | 7.3 | 1.14 | 0.41 | 5.5 | 12.1 |
| | Bif. 3 | 21.5 | 0.051 | 10.7 | 0.55 | 297 | 6.6 | 0.68 | 0.37 | 5.5 | 10.9 |
| | Bif. 4 | 9.5 | 0.040 | 12.8 | 0.65 | 86 | 8.4 | 2.21 | 1.30 | 6.1 | 14.1 |
| | Bif. 6 | 16.5 | 0.034 | 11.4 | 0.58 | 134 | 7.2 | 1.18 | 0.57 | 5.6 | 12.9 |
| Drau | | 27.4 | 0.210 | 16.4 | 0.63 | 263 | 3.6 | 0.15 | 1.03 | 22.3 | 61.4 |

The critical aspect ratio $\beta_C$ turns out to be significantly higher than the corresponding value $\beta_C^\infty$ calculated considering for the sole bifurcation (Bolla Pittaluga et al., 2003), which highlights the significant effect of the confluence on the stability of the system.

on the mechanism of gravitational pull. If the connecting branches are sufficiently short (i.e., $\Lambda \simeq 1.6$), this effect is sufficient to stabilize the bifurcation-confluence loop, even in the limiting case $r = 0$.

### 6.4. Relevance in Fluvial Systems

From the results reported in Figure 11, we can derive an estimate of the magnitude of the channel length $L$ for which the presence of a downstream confluence plays an in important role in determining the stability of the bifurcation. Specifically, we can see that values of $\Lambda$ of order one are needed to produce a significant interaction between the effect of the bifurcation and that of the confluence. Since $c_0 \sim 10$, the corresponding values of $L^*$ are of order 100, which, assuming $W_0/D_0 \sim 10$, gives length-to-width ratios $L/W_0$ of order 10. Similar values are often observed in natural settings, as reported, e.g., by Nanson and Knighton (1996), who measured the ratio between island length and main channel width in different types of multithread rivers (see their Figure 2). Furthermore, it is worth noting that comparable values of $L/W_0$ result from the empirical expressions proposed by Hundey and Ashmore (2009) for the link length (i.e., the mean length of subsequent confluence-bifurcation units, see Ashmore, 2001) of braided systems.

To test more directly the possible effect of the presence of a downstream confluence in natural bifurcations, we take a few examples from the literature, where data for different channel loops in gravel bed streams are reported. Specifically, we consider four natural cases in the wandering Renous River (Canada), studied in detail by Burge (2006), and the case of an artificial, side-channel reconstruction along the Drau River (Austria, see Figure 1c), which has been investigated, among the others, by Formann et al. (2007). For a specific estimation of the parameter $\alpha$, we adopt the method of Redolfi et al. (2019), which is based on the assumption that $\beta_C^\infty$ should be equal to the resonant threshold value $\beta_R$. Results of the linear analysis, reported in Table 1, reveal that the critical aspect ratio $\beta_C$ is nearly doubled with respect to the value $\beta_C^\infty$ given by the formulation of Bolla Pittaluga et al. (2003). This highlights the important role played by the downstream confluence in determining the stability of the system and controlling its long-term configuration.

### 6.5. Limitations and Potential for Further Studies

For the sake of simplicity, we limited our analysis to a symmetrical case, where the connecting channels have the same width and length, and reconnect at the confluence with the same angle. Moreover, we assumed that the width of the main upstream and downstream branch is the same, and equal to twice the width of the two secondary channels. However, these hypotheses can be easily relaxed, as the model is formulated in general terms, with values of angles, lengths and widths that can be freely assigned.

The steady assumption could also be relaxed by considering an evolving system, where the sediment flux is not constant along the channels. A first approximation could be obtained by assuming that the channels evolve as a sequence of quasi-equilibrium states (e.g., Bolla Pittaluga et al., 2003), while a more general approach would require a description of the channels through a one-dimensional differential problem (see the cell discretization of Salter et al. (2018)). Studying the unsteady dynamics of the bifurcation-confluence

loop would allow for exploring the initial transitory phase, the response to discharge variations, and the interaction with time-dependent forcing effects due to the migration of bars (e.g., Bertoldi et al., 2009b) or downstream tidal fluctuations. Moreover, the unsteady analysis would allow for detecting the presence of possible autogenic oscillations, similar to those revealed by Salter et al. (2018, 2019) for bifurcations in depositional river deltas.

The present model is based on the assumption of fixed banks. If this can be considered valid for the case of artificial structures (see Figure 1d), this is never exactly the case for natural bifurcations. However, we expect that the approach is more generally applicable to cases where bank erosion processes (and the associated time scale of planform evolution) are comparatively slow with respect to the bed adaptation (see Monegaglia & Tubino, 2019). This condition is typically fulfilled in anastomosing rivers, where the individual channels, often separated by vegetated islands, are usually persisting for decades or centuries (Nanson & Knighton, 1996). Conversely, more caution needs to be taken when applying our approach to braided channels, where the lateral channel and confluence migration can be relatively fast (see Ashmore, 2013; Dixon et al., 2018; Sambrook Smith et al., 2019).

Lastly, the empirical expressions for the interfacial shear and separation coefficients proposed by Shabayek et al. (2002) and Luo et al. (2018) (see Equation 20) are based on experimental data taken in conditions far from those observed in natural confluences. Our comparison with the field experiment of Sukhodolov and Sukhodolova (2019) suggests that this laboratory-based coefficients are also adequate to represent (at least qualitatively) the confluence dynamics in much more realistic conditions. However, there is a demand for a more specific calibration of the coefficients $K_{b,c}$ and $K_I$, depending on confluence geometry, bed morphology, and flow characteristics. For example, in cases where the junction corners are not sharp but characterized by a more gentle curvature, as typical of natural settings (Ashmore et al., 1992), the importance of the separation zone is likely to reduce, and therefore the appropriate value of the coefficients $K_{b,c}$ is probably lower. Similarly, when the bed is erodible, the interfacial shear coefficient $K_I$, physically representing the lateral exchange of momentum along the shear layer, may significantly vary with respect to the value 0.21 adopted in the present formulation. However, from a qualitatively point of view, a value of $K_I$ such that $\Delta H > 0$ (see Figure 7b) is highly expectable, in as much as the interaction between the bed morphology and the flow field that defines the shear layer structure is likely to even reinforce the lateral momentum exchange and increase the shear stress at the interface.

## 7. Conclusions

In this work, we propose a novel theoretical modeling framework for investigating the effect of a downstream confluence on the stability of a river bifurcation. On the basis of model results and their interpretation, we can draw the following conclusions:

1. The proposed confluence model allows for predicting differences in the water surface elevation between the two merging channels, depending on geometrical and hydrodynamical conditions. The model reveals that the dominating branch (i.e., that carrying more water and sediment) is subject to a slightly higher water surface elevation, showing a water level asymmetry that is proportional to the square of the Froude number
2. The increase in the water surface elevation at the confluence node tends to reduce the slope of the dominating branch, which therefore becomes "less dominant." This negative feedback is responsible for a clear stabilizing effect on the bifurcation-confluence loop
3. The linear analysis of the coupled system allows for identifying the key controlling parameters of the stability of a bifurcation-confluence loop. The stabilizing effect of the confluence turns out to depend on the ratio between the length of the connecting channels and the average water depth, while it is almost independent of channel slope and Froude number, which clearly shows that the backwater length is not the correct scaling length for this kind of systems
4. The effect of the confluence is potentially able to stabilize the bifurcation-confluence loop even in conditions where the classic mechanism described by Bolla Pittaluga et al. (2003) (i.e., the topographical effect related to the gravitational pull on the sediment transport) is very weak, as in the case when most of the sediment is transported in suspension

5. Typical lengths of connecting branches observed in natural rivers suggest that the effect of the confluence is usually important in determining the stability of natural bifurcation-confluence loops. Noteworthy, this effect is equally relevant in low-gradient channels, despite the fact that variations of the water surface elevation, being proportional to the square of the Froude number, may appear as negligible

In our analysis, we restricted the attention to the simplest geometrical configuration. However, our model is also suitable for examining the effect of different channel lengths, widths, and confluence angles. Moreover, the proposed model could allow for investigating the stability of a free-forced system, where the presence of "external" disturbances (e.g., downstream-migrating bars in the upstream channel) may alter the stability of the loop, possibly leading to multiple, counter-intuitive solutions (Redolfi et al., 2019). Ultimately, this work provides a relatively simple, theoretically based, modeling framework that can be used to design and interpret results from physical experiments and numerical simulations.

## Appendix A: Streamwise Momentum Equation on a Curved Control Volume

The nodal point relation we propose, as well as the original formulation of Shabayek et al. (2002), are based on the momentum balance on the curved control volumes illustrated in Figure 5. The application of such a balance is not straightforward, due to the fact that forces and momentum fluxes are acting in different directions. Therefore, we need to formalize the procedure adopted to derive an integral momentum equation for an arbitrary, curved control volume. For the sake of notational compactness, we here neglect the effects of the bottom friction, as justified when the domain length is relatively short.

As illustrated in Figure A1, we consider a generic open channel, and we define a volume whose lateral boundaries follow the flow streamlines (or the channel banks). For each point in the domain, it is possible to define cross sections so that the associated cross-sectionally averaged momentum vector ($\vec{M}$) is always orthogonal to the sections themselves. This allows us to draw a curvilinear axis that is everywhere aligned with the momentum vector, and to define the coordinate $s \in [0, l]$ as the distance along the axis itself.

With reference to Figure A1, we consider a slice of infinitesimal width $ds$, and we apply the momentum equation under assumption of steady flow conditions. Once projected along the direction of the axis (locally defined by the unit vector $\hat{s}$), the momentum balance reads:

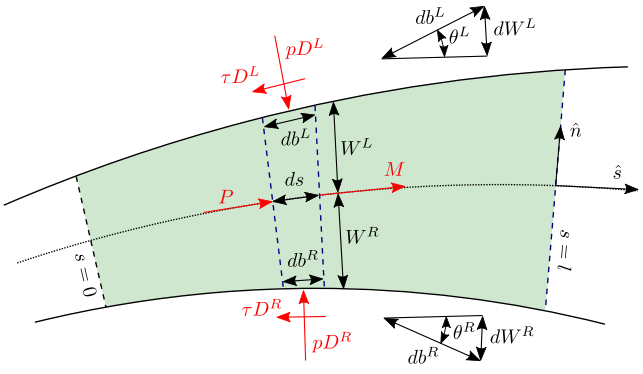


**Figure A1.** Definition of the curved control volume (shaded area) and forces acting on each elementary slice (red arrows), where $M$ is the momentum flux and $P$ is the pressure force exerted on the cross section. The pressure $p$ and the shear stress $\tau$, once multiplied by the water depth $D$, represent the forces (per unit length $db$), acting on the left and on the right sides ($^L$ and $^R$ superscripts, respectively). The dotted line indicates the axis, whose local direction is indicated by the unit vector $\hat{s}$; the dashed lines indicate cross sections, which follow the orthogonal direction $\hat{n}$. Upstream and downstream cross sections are identified by values of the curvilinear coordinate $s = 0$ and $s = l$, respectively.

$$\begin{aligned} dM &= -dP + pD^L \sin\theta^L db^L + pD^R \sin\theta^R db^R \\ &\quad -\tau D^L \cos\theta^L db^L - \tau D^R \cos\theta^R db^R + dP^F, \end{aligned} \tag{A1}$$

where $b$ is the curvilinear distance along the lateral boundaries, which are inclined by an angle $\theta$ with respect to the direction $\hat{s}$. The last term of Equation A1, $dP^F$, indicates the streamwise pressure force acting on the bed, which can be calculated as:

$$dP^F = \int_{n=-W_R}^{W_L} p^F \frac{\partial \eta}{\partial s} ds dn, \tag{A2}$$

where $p^F$ is the bed pressure and $d\eta$ represents the bed elevation difference in the streamwise direction $\hat{s}$. It is worth noticing that if the bottom is simply formed by a sloping plane, as typically the case in fixed bed experiments, it is possible to simply rotate the system of reference to obtain $\eta = \text{const}$ along the entire domain, which gives a vanishing streamwise pressure force $P^F$. Considering the trigonometric relation $dW = db\sin\theta$, and defining the streamwise component of the shear stress $\tau_s = \tau\cos\theta$, Equation A1 reads:

$$dM = -dP + pD^L dW^L + pD^R dW^R - \tau_s D^L db^L - \tau_s D^R db^R + dP^F. \tag{A3}$$

To obtain the global momentum balance for the volume illustrated in Figure A1, we integrate Equation A3 along the streamwise direction, which gives:

$$\int_{s=0}^{l} dM = \int_{s=0}^{l} \left[ -dP + pD^L dW^L + pD^R dW^R - \tau_s D^L db^L - \tau_s D^R db^R + dP^F \right]. \tag{A4}$$

Assuming that the forces per unit length $pD$ and $\tau_s D$ do not significantly vary with respect to their averaged values along the lateral boundaries ($\overline{pD}$ and $\overline{\tau D}$), they can be moved outside the integral, which gives

$$\begin{aligned} M^{OUT} - M^{IN} &= P^{IN} - P^{OUT} + \overline{pD}^L \Delta W^L + \overline{pD}^R \Delta W^R \\ &\quad -\overline{\tau_s D}^L l^L - \overline{\tau_s D}^R l^R + P^F, \end{aligned} \tag{A5}$$

where $\Delta W^L$ and $\Delta W^R$ represent the change of width on the left and on the right sides of the axis, so that their sum $\Delta W$ represents the width variation from the upstream ($s = 0$) to the downstream ($s = l$) cross sections. More generally, the variability of depth, pressure, and shear stress along the lateral boundaries can be taken into account by expressing the momentum balance (Equation A4) as:

$$\begin{aligned} M^{OUT} - M^{IN} &= P^{IN} - P^{OUT} + \psi^L \overline{pD}^L \Delta W^L + \psi^R \overline{pD}^R \Delta W^R \\ &\quad -\chi^L \overline{\tau_s D}^L \Delta b^L - \chi^R \overline{\tau_s D}^R \Delta b^R + P^F, \end{aligned} \tag{A6}$$

where $\Delta b$ indicates the length of the lateral boundaries, and $\psi$ and $\chi$ are the correction coefficients defined as:

$$\psi := \frac{\int_{s=0}^{l} pD dW}{\overline{pD}\Delta W}, \quad \chi := \frac{\int_{s=0}^{l} \tau_s D db}{\overline{\tau_s D}\Delta b}. \tag{A7}$$

Lastly, the total pressure force acting on the bed, $P^F$, can be computed by integrating Equation A9 along the streamwise direction:

$$P^F = \int_{s=0}^{l} dP^F = \int_{s=0}^{l} \int_{n=-W_R}^{W_L} p^F \frac{\partial \eta}{\partial s} ds dn, \tag{A8}$$

which, assuming relatively small spatial variations of the bed pressure, $p^F$, reads:

$$P^F = p^F \int_{s=0}^{l} \int_{n=-W_R}^{W_L} \frac{\partial \eta}{\partial s} ds dn = p^F \overline{S} A, \tag{A9}$$

where $A$ is the planimetric area of the control volume (shaded area of Figure A1), and $\overline{S}$ indicates the average downstream slope of the bed within the volume.

## Data Availability Statement

A reprinted version of the Figure 2 of Shabayek et al. (2002), where experimental data used for the calibration of the empirical coefficients $K_{b,c}$ and $K_I$ are illustrated, is reported in supporting information. A Matlab code for computing the marginal stability conditions for the bifurcation-confluence loop is made available in a public repository at https://doi.org/10.5281/zenodo.3939277.

**Acknowledgments**
This work has been supported by the Italian Ministry of Education, University and Research (MIUR) in the frame of the "Departments of Excellence" grant L. 232/2016 and by the "Agenzia Provinciale per le Risorse Idriche e l'Energia" (APRIE) of the Province of Trento (Italy). The work has benefited from the thoughtful comments by Maarten Kleinhans and Gerard Salter.

## References

Ashmore, P. (2001). Braiding phenomena: Statics and kinetics. In M. P. Mosley (Ed.), *Gravel Bed Rivers V* (pp. 95–121). Wellington: New Zealand Hydrological Society.

Ashmore, P. (2013). Morphology and dynamics of braided rivers. *Treatise on Geomorphology*, *9*, 289–312. https://doi.org/10.1016/B978-0-12-374739-6.00242-6

Ashmore, P. E., Ferguson, R. I., Prestegaard, K. L., Ashworth, P. J., & Paola, C. (1992). Secondary flow in anabranch confluences of a braided, gravel-bed stream. *Earth Surface Processes and Landforms*, *17*(3), 299–311. https://doi.org/10.1002/esp.3290170308

Ashworth, P. J. (1996). Mid-channel bar growth and its relationship to local flow strength and direction. *Earth Surface Processes and Landforms*, *21*(2), 103–123. https://doi.org/10.1002/(Sici)1096-9837(199602)21:2<103::Aid-Esp569>3.0.Co;2-O

Ashmore, P., & Parker, G. (1983). Confluence scour in coarse braided streams. *Water Resources Research*, *19*(2), 392–402. https://doi.org/10.1029/WR019i002p00392

Baar, A. W., de Smit, J., Uijttewaal, W. S., & Kleinhans, M. G. (2018). Sediment transport of fine sand to fine gravel on transverse bed slopes in rotating annular flume experiments. *Water Resources Research*, *54*, 19–45. https://doi.org/10.1002/2017WR020604

Bertoldi, W., & Tubino, M. (2007). River bifurcations: Experimental observations on equilibrium configurations. *Water Resources Research*, *43*, W10437. https://doi.org/10.1029/2007WR005907

Bertoldi, W., Zanoni, L., Miori, S., Repetto, R., & Tubino, M. (2009). Interaction between migrating bars and bifurcations in gravel bed rivers. *Water Resources Research*, *45*, W06418. https://doi.org/10.1029/2008WR007086

Bertoldi, W., Zanoni, L., & Tubino, M. (2009). Planform dynamics of braided streams. *Earth Surface Processes and Landforms*, *34*(4), 547–557. https://doi.org/10.1002/esp.1755

Best, J. L. (1986). The morphology of river channel confluences. *Progress in Physical Geography*, *10*(2), 157–174. https://doi.org/10.1177/030913338601000201

Best, J. L. (1988). Sediment transport and bed morphology at river channel confluences. *Sedimentology*, *35*(3), 481–498. https://doi.org/10.1111/j.1365-3091.1988.tb00999.x

Best, J. L., & Reid, I. (1984). Separation zone at open-channel junctions. *Journal of Hydraulic Engineering*, *110*(11), 1588–1594. https://doi.org/10.1061/(ASCE)0733-9429(1984)110:11(1588)

Best, J. L., & Rhoads, B. L. (2008), Sediment transport, bed morphology and the sedimentology of river channel confluences. In S. P. Rice, B. L. Rhoads, & A. G. Roy (Eds.), *River Confluences, Tributaries and the Fluvial Network* (chap. 4, p. 456). West Sussex, UK: John Wiley & Sons. https://doi.org/10.1002/9780470760383

Best, J. L., & Roy, A. G. (1991). Mixing-layer distortion at the confluence of channels of different depth. *Nature*, *350*(6317), 411–413. https://doi.org/10.1038/350411a0

Biron, P., Best, J. L., & Roy, A. G. (1996). Effects of bed discordance on flow dynamics at open channel confluences. *Journal of Hydraulic Engineering*, *122*(12), 676–682. https://doi.org/10.1061/(ASCE)0733-9429(1996)122:12(676)

Biron, P., Roy, A., Best, J. L., & Boyer, C. J. (1993). Bed morphology and sedimentology at the confluence of unequal depth channels. *Geomorphology*, *8*(2–3), 115–129. https://doi.org/10.1016/0169-555X(93)90032-W

Biron, P. M., & Lane, S. N. (2008). Modeling hydraulics and sediment transport at river confluences. In S. P. Rice, B. L. Rhoads, & A. G. Roy (Eds.), *River Confluences, Tributaries and the Fluvial Network* (chap. 3, p. 456). West Sussex, UK: John Wiley & Sons. https://doi.org/10.1002/9780470760383

Bolla Pittaluga, M., Coco, G., & Kleinhans, M. G. (2015). A unified framework for stability of channel bifurcations in gravel and sand fluvial systems. *Geophysical Research Letters*, *42*, 7521–7536. https://doi.org/10.1002/2015GL065175

Bolla Pittaluga, M., Repetto, R., & Tubino, M. (2003). Correction to "Channel bifurcation in braided rivers: Equilibrium configurations and stability". *Water Resources Research*, *39*(3), 1046. https://doi.org/10.1029/2003WR002754

Boyer, C., Roy, A. G., & Best, J. L. (2006). Dynamics of a river channel confluence with discordant beds: Flow turbulence, bed load sediment transport, and bed morphology. *Journal of Geophysical Research*, *111*, F04007. https://doi.org/10.1029/2005JF000458

Bradbrook, K., Lane, S. N., Biron, P., & Roy, A. (2001). Role of bed discordance at asymmetrical river confluences. *Journal of Hydraulic Engineering*, *127*(5), 351–368.

Bradbrook, K. F., Lane, S. N., & Richards, K. S. (2000). Numerical simulation of three-dimensional, time-averaged flow structure at river channel confluences. *Water Resources Research*, *36*(9), 2731–2746. https://doi.org/10.1029/2000WR900011

Burge, L. M. (2006). Stability, morphology and surface grain size patterns of channel bifurcation in gravel-cobble bedded anabranching rivers. *Earth Surface Processes and Landforms*, *31*(10), 1211–1226. https://doi.org/10.1002/esp.1325

Chadwick, A. J., Lamb, M. P., Moodie, A. J., Parker, G., & Nittrouer, J. A. (2019). Origin of a preferential avulsion node on lowland river deltas. *Geophysical Research Letters*, *46*, 4267–4277. https://doi.org/10.1029/2019GL082491

Coelho, M. M. L. P. (2015). Experimental determination of free surface levels at open-channel junctions. *Journal of Hydraulic Research*, *53*(3), 394–399. https://doi.org/10.1080/00221686.2015.1013513

Collas, F., Buijse, A., van den Heuvel, L., van Kessel, N., Schoor, M., Eerden, H., & Leuven, R. (2018). Longitudinal training dams mitigate effects of shipping on environmental conditions and fish density in the littoral zones of the river Rhine. *The Science of the Total Environment*, *619–620*, 1183–1193. https://doi.org/10.1016/j.scitotenv.2017.10.299

de Ruijsscher, T. V., Vermeulen, B., & Hoitink, A. J. (2020). Diversion of flow and sediment toward a side channel separated from a river by a longitudinal training dam. *Water Resources Research*, *56*, e2019WR026750. https://doi.org/10.1029/2019WR026750

Dixon, S. J., Sambrook Smith, G. H., Best, J. L., Nicholas, A. P., Bull, J. M., Vardy, M. E., et al. (2018). The planform mobility of river channel confluences: Insights from analysis of remotely sensed imagery. *Earth-Science Reviews*, *176*, 1–18. https://doi.org/10.1016/j.earscirev.2017.09.009

Edmonds, D. A., & Slingerland, R. L. (2008). Stability of delta distributary networks and their bifurcations. *Water Resources Research*, *44*, W09426. https://doi.org/10.1029/2008WR006992

Engelund, F., & Hansen, E. (1967). *A Monograph on Sediment Transport in Alluvial Streams*. Copenhagen K: Technical University of Denmark.

Federici, B., & Paola, C. (2003). Dynamics of channel bifurcations in noncohesive sediments. *Water Resources Research*, *39*(6), 1162. https://doi.org/10.1029/2002WR001434

Formann, E., Habersack, H. M., & Schober, S. (2007). Morphodynamic river processes and techniques for assessment of channel evolution in Alpine gravel bed rivers. *Geomorphology*, *90*(3–4), 340–355. https://doi.org/10.1016/j.geomorph.2006.10.029

Fraccarollo, L., & Capart, H. (2002). Riemann wave description of erosional dam-break flows. *Journal of Fluid Mechanics*, *461*, 183–228. https://doi.org/10.1017/S0022112002008455

Graf, W. L. (2006). Downstream hydrologic and geomorphic effects of large dams on American rivers. *Geomorphology*, *79*(3–4), 336–360. https://doi.org/10.1016/j.geomorph.2006.06.022

Grenfell, M., Aalto, R., & Nicholas, A. (2012). Chute channel dynamics in large, sand-bed meandering rivers. *Earth Surface Processes and Landforms*, *37*(3), 315–331. https://doi.org/10.1002/esp.2257

Gurram, S., Karki, K., & Hager, W. (1997). Subcritical junction flow. *Journal of Hydraulic Engineering*, *123*(5), 447–455.

Habersack, H., & Piégay, H. (2007). 27 river restoration in the Alps and their surroundings: Past experience and future challenges. In H. Habersack, H. Piégay, & M. Rinaldi (Eds.), *Gravel-Bed Rivers VI: From Process Understanding to River Restoration* (pp. 703–737). Amsterdam: Elsevier B.V. https://doi.org/10.1016/S0928-2025(07)11161-5

Hager, W. (1987). Separation zone at open-channel junctions. *Journal of Hydraulic Engineering*. *113*(4), 539–543. https://doi.org/10.1061/(ASCE)0733-9429(1987)113:4(543)

Hsu, C.-C., Lee, W.-J., & Chang, C.-H. (1998). Subcritical open-channel junction flow. *Journal of Hydraulic Engineering*, *124*(8), 847–855. https://doi.org/10.1061/(ASCE)0733-9429(1998)124:8(847)

Hundey, E. J., & Ashmore, P. E. (2009). Length scale of braided river morphology. *Water Resources Research*, *45*, W08409. https://doi.org/10.1029/2008WR007521

Ikeda, S., Parker, G., & Sawai, K. (1981). Bend theory of river meanders. Part 1. Linear development. *Journal of Fluid Mechanics*, *112*, 363–377. https://doi.org/10.1017/S0022112081000451

Keulegan, G. H. (1938). Laws of turbulent flow in open channels. *Journal of Research of the National Bureau of Standards*, *21*, 707–741. https://doi.org/10.6028/jres.021.039

Kleinhans, M. G., de Haas, T., Lavooi, E., & Makaske, B. (2012). Evaluating competing hypotheses for the origin and dynamics of river anastomosis. *Earth Surface Processes and Landforms*, *37*(12), 1337–1351. https://doi.org/10.1002/esp.3282

Kleinhans, M. G., Jagers, H. R., Mosselman, E., & Sloff, C. J. (2008). Bifurcation dynamics and avulsion duration in meandering rivers by one-dimensional and three-dimensional models. *Water Resources Research*, *44*, W08454. https://doi.org/10.1029/2007WR005912

Lane, S. N., Bradbrook, K., Richards, K., Biron, P., & Roy, A. (2000). Secondary circulation cells in river channel confluences: Measurement artifacts or coherent flow structures? *Hydrological Processes*, *14*(11–12), 2047–2071. https://doi.org/10.1002/1099-1085(20000815/30)14:11/12¡2047::aid-hyp54¿3.0.co;2-4

Leclair, S. F., & Roy, A. G. (1997). Variabilité de la morphologie et des structures sédimentaires du lit d'un confluent de cours d'eau discordant en période d'étiage. *Géographie Physique et Quaternaire*, *51*(2), 125–139. https://doi.org/10.7202/033114ar

Leite Ribeiro, M., Blanckaert, K., Roy, A. G., & Schleiss, A. J. (2012). Flow and sediment dynamics in channel confluences. *Journal of Geophysical Research*, *117*, F01035. https://doi.org/10.1029/2011JF002171

Le, T., Crosato, A., Mosselman, E., & Uijttewaal, W. (2018). On the stability of river bifurcations created by longitudinal training walls. Numerical investigation. *Advances in Water Resources*, *113*, 112–125. https://doi.org/10.1016/j.advwatres.2018.01.012

Luo, H., Fytanidis, D. K., Schmidt, A. R., & García, M. H. (2018). Comparative 1D and 3D numerical investigation of open-channel junction flows and energy losses. *Advances in Water Resources*, *117*, 120–139. https://doi.org/10.1016/j.advwatres.2018.05.012

Miori, S., Hardy, R. J., & Lane, S. N. (2012). Topographic forcing of flow partition and flow structures at river bifurcations. *Earth Surface Processes and Landforms*, *37*(6), 666–679. https://doi.org/10.1002/esp.3204

Miori, S., Repetto, R., & Tubino, M. (2006). A one-dimensional model of bifurcations in gravel bed channels with erodible banks. *Water Resources Research*, *42*, W11413. https://doi.org/10.1029/2006WR004863

Monegaglia, F., & Tubino, M. (2019). The hydraulic geometry of evolving meandering rivers. *Journal of Geophysical Research: Earth Surface*, *124*, 2723–2748. https://doi.org/10.1029/2019JF005309

Moodie, A. J., Nittrouer, J. A., Ma, H., Carlson, B. N., Chadwick, A. J., Lamb, M. P., & Parker, G. (2019). Modeling deltaic lobe-building cycles and channel avulsions for the Yellow river delta, China. *Journal of Geophysical Research: Earth Surface*, *124*, 2438–2462. https://doi.org/10.1029/2019JF005220

Mosley, M. P. (1976). An experimental study of channel confluences. *The Journal of Geology*, *84*(5), 535–562. https://doi.org/10.1086/628230

Nanson, G. C., & Knighton, D. A. (1996). Anabranching rivers: Their cause, character and classification. *Earth Surface Processes and Landforms*, *21*(3), 217–239. https://doi.org/10.1002/(SICI)1096-9837(199603)21:3<217::AID-ESP611>3.0.CO;2-U

Paola, C. (1997). When streams collide. *Nature*, *387*, 232–233. https://doi.org/10.1080/08940889508602829

Paola, C., & Mohrig, D. (1996). Palaeohydraulics revisited: Palaeoslope estimation in coarse-grained braided rivers. *Basin Research*, *8*, 243–254. https://doi.org/10.1046/j.1365-2117.1996.00253.x

Parker, G. (1990). Surface-based bedload transport relation for gravel rivers. *Journal of Hydraulic Research*, *28*(4), 417–436. https://doi.org/10.1080/00221689009499058

Parker, G., Wilcock, P. R., Paola, C., Dietrich, W. E., & Pitlick, J. (2007). Physical basis for quasi-universal relations describing bankfull hydraulic geometry of single-thread gravel bed rivers. *Journal of Geophysical Research*, *112*, F04005. https://doi.org/10.1029/2006JF000549

Ragno, N., Tambroni, N., & Bolla Pittaluga, M. (2020). Effect of small tidal fluctuations on the stability and equilibrium configurations of bifurcations. *Journal of Geophysical Research: Earth Surface*, *125*, e2020JF005584. https://doi.org/10.1029/2020JF005584

Rajaratnam, N. (1976). *Turbulent Jets* (pp. 304). Amsterdam: Elsevier.
Redolfi, M., Zolezzi, G., & Tubino, M. (2016). Free instability of channel bifurcations and morphodynamic influence. *Journal of Fluid Mechanics*, *799*, 476–504. https://doi.org/10.1017/jfm.2016.389
Redolfi, M., Zolezzi, G., & Tubino, M. (2019). Free and forced morphodynamics of river bifurcations. *Earth Surface Processes and Landforms*, *44*(4), 973–987. https://doi.org/10.1002/esp.4561
Rhoads, B. L., & Sukhodolov, A. (2004). Spatial and temporal structure of shear layer turbulence at a stream confluence. *Water Resources Research*, *40*, W06304. https://doi.org/10.1029/2003WR002811
Salter, G., Paola, C., & Voller, V. R. (2018). Control of delta avulsion by downstream sediment sinks. *Journal of Geophysical Research: Earth Surface*, *123*, 142–166. https://doi.org/10.1002/2017JF004350
Salter, G., Voller, V. R., & Paola, C. (2019). How does the downstream boundary affect avulsion dynamics in a laboratory bifurcation? *Earth Surface Dynamics Discussions*, *7*, 911–927. https://doi.org/10.5194/esurf-2019-26
Sambrook Smith, G. H., Nicholas, A. P., Best, J. L., Bull, J. M., Dixon, S. J., Goodbred, S., et al. (2019). The sedimentology of river confluences. *Sedimentology*, *66*(2), 391–407. https://doi.org/10.1111/sed.12504
Samuels, P. G. (1989), Backwater lengths in rivers. *Proceedings of the Institution of Civil Engineers*, *87*(4), 571–582. https://doi.org/10.1680/iicep.1989.3779
Schaffranek, R. W., Baltzer, R. A., & Goldberg, D. E. (1981). *A Model for Simulation of Flow in Singular and Interconnected Channels*, Washington, DC: USGS Publications.
Seminara, G., Bolla Pittaluga, M., & Tambroni, N. (2012). Morphodynamic equilibrium of tidal channels. *Environmental Fluid Mechanics: Memorial Volume in Honour of Prof. Gerhard H. Jirka*, (Ch 8, pp. 153–174. https://doi.org/10.1201/b12283
Shabayek, S., Steffler, P., & Hicks, F. (2002). Dynamic model for subcritical combining flows in channel junctions. *Journal of Hydraulic Engineering*, *128*(9), 821–828. https://doi.org/10.1061/(ASCE)0733-9429(2002)128:9(821)
Siviglia, A., Stecca, G., Vanzo, D., Zolezzi, G., Toro, E. F., & Tubino, M. (2013). Numerical modeling of two-dimensional morphodynamics with applications to river bars and bifurcations. *Advances in Water Resources*, *52*, 243–260. https://doi.org/10.1016/j.advwatres.2012.11.010
Sukhodolov, A. N., & Sukhodolova, T. A. (2019). Dynamics of flow at concordant gravel bed river confluences: Effects of junction angle and momentum flux ratio. *Journal of Geophysical Research: Earth Surface*, *124*, 588–615. https://doi.org/10.1029/2018JF004648
Taylor, E. H. (1944). Flow characteristics at rectangular open-channel junctions. *Transaction of ASCE*, *109*, 893–912.
Tong-Huan, L., Yi-Kui, W., Xie-Kang, W., Huan-Feng, D., & Xu-Feng, Y. (2020). Morphological environment survey and hydrodynamic modeling of a large bifurcation-confluence complex in Yangtze River, China. *The Science of the Total Environment*, *737*, 139705. https://doi.org/10.1016/j.scitotenv.2020.139705
van Denderen, R. P., Schielen, R. M., Blom, A., Hulscher, S. J., & Kleinhans, M. G. (2018). Morphodynamic assessment of side channel systems using a simple one-dimensional bifurcation model and a comparison with aerial images. *Earth Surface Processes and Landforms*, *43*(6), 1169–1182. https://doi.org/10.1002/esp.4267
Wang, Z. B., De Vries, M., Fokkink, R. J., & Langerak, A. (1995). Stability of river bifurcations in 1D morphodynamic models. *Journal of Hydraulic Research*, *33*(6), 739–750. https://doi.org/10.1080/00221689509498549
Wiggins, S. (2003). *Introduction to Applied Nonlinear Dynamical Systems and Chaos*, New York, NY: Springer. https://doi.org/10.2307/3620310
Wilkerson, G. V., & Parker, G. (2011). Physical basis for quasi-universal relationships describing bankfull hydraulic geometry of sand-bed rivers. *Journal of Hydraulic Engineering*, *137*(7), 739–753. https://doi.org/10.1061/(ASCE)HY.1943-7900.0000352
Wohl, E., Lane, S. N., & Wilcox, A. C. (2015). The science and practice of river restoration. *Water Resources Research*, *51*, 5974–5997. https://doi.org/10.1002/2014WR016874
Zolezzi, G., Bertoldi, W., & Tubino, M. (2006). Morphological analysis and prediction of river bifurcations. In G. H. Best, J. L. Bristow, & C. S. Petts (Eds.), Braided Rivers: Process, Deposits, Ecology and Management (Vol. 36, pp. 233–256). Oxford, UK: Blackwell. https://doi.org/10.1002/9781444304374.ch11
Zolezzi, G., Luchi, R., & Tubino, M. (2012). Modeling morphodynamic processes in meandering rivers with spatial width variations. *Reviews of Geophysics*, *50*, RG4005. https://doi.org/10.1029/2012RG000392
Zolezzi, G., & Seminara, G. (2001). Downstream and upstream influence in river meandering. Part 1. General theory and application to overdeepening. *Journal of Fluid Mechanics*, *438*, 183–211. https://doi.org/10.1017/S002211200100427X